EUMETSAT ECMWF

EUMETSAT/ECMWF Fellowship Programme Research Report

62

Assimilating FY-3E MWHS-2 observations, and assessing all-sky humidity sounder thinning scales

Liam Steele, Niels Bormann and David Duncan

December 2023

Series: EUMETSAT/ECMWF Fellowship Programme Research Reports

A full list of ECMWF Publications can be found on our web site under:
http://www.ecmwf.int/en/publications/

Contact: library@ecmwf.int

European Centre for Medium Range Weather Forecasts, Shinfield Park, Reading, RG2 9AX, UK

Abstract

Microwave observations sensitive to temperature and water vapour are one of the most important observation types in the four-dimensional variational assimilation scheme used at ECMWF. In this report we assess the forecast benefits of assimilating early-morning data from the Micro-Wave Humidity Sounder-2 (MWHS-2) instrument aboard the Fengyun-3E (FY-3E) satellite, and also investigate the optimal spatial thinning scale for microwave humidity sounder observations. These investigations will help to inform on how to extract the most benefit from both current and future microwave sounder instruments, such as those on the upcoming Metop second generation satellites and the EPS-Sterna constellation. We find that assimilating the FY-3E MWHS-2 data leads to short- and medium-range forecast improvements, particularly in the southern hemisphere, which are statistically-significant out to day 3. While some of the forecast improvement is due to lower noise compared to previous incarnations of the same instrument, dedicated assimilation experiments demonstrate that the early morning orbit of FY-3E, which complements the local times of other assimilated data, also plays a role. Due to the observed forecast improvements, the FY-3E MWHS-2 instrument became operationally active on 22 February 2023. We also find that the current spatial thinning scale for humidity sounding observations of 111 km can be reduced to ∼55 km. This results in less data being discarded and gives an improvement to forecasts out to day 3. Thinning scales smaller than ∼55 km result in degraded forecasts, likely due to neglected spatial observation error correlations.

Plain language summary

In order to produce weather forecasts we first need to know the current state of the Earth's atmosphere and surface. To do this, ECMWF uses a technique called data assimilation, in which a large number of observations of the Earth system are combined with a computer model. This creates the initial conditions from which a 10 day forecast is performed.

In this report we add observations from a new satellite instrument - the Micro-Wave Humidity Sounder-2 instrument aboard the Fengyun-3E satellite - to assess whether this improves our weather forecast. We find that including this data improves the forecast out to day 3, with the signal becoming less clear for longer forecast times. The largest improvements are seen in the forecast for the southern hemisphere. We attribute the forecast improvement to two reasons: Firstly, the data from the new instrument are of better quality than the older instruments. Secondly, the new instrument takes measurements at a different time of day, which provides complementary information on the state of the atmosphere. On 22 February 2023 this new instrument was included in the data assimilation system which is used to make ECMWF's weather forecasts.

While ECMWF receives millions of observations each day, we cannot use all this data. This is because errors in one observation can affect errors in another observation (known as error correlation), which is difficult to calculate. As such, we remove data so that the observations are a certain distance apart and we can ignore correlated errors. In this report we test multiple different distances between observations, and determine that we can use more data than we currently do, by reducing the distance from around 111 km to 55 km. If we try to use data spaced more closely than 55 km the weather forecast gets worse, which is likely due to us neglecting correlated errors.

The investigations performed in this report help guide us on how best to use microwave sounder data, which improves our use of data from currently-assimilated instruments, as well as data from instruments on upcoming satellites, such as EUMETSATs Metop second generation satellites and the EPS-Sterna constellation, due to be launched in the next few years.

1 Introduction

Microwave observations sensitive to temperature and water vapour are routinely used in numerical weather prediction (NWP), and are one of the most important observation types in the assimilation scheme used at ECMWF (Geer *et al.*, 2017). While humidity sounders are sensitive to water vapour, cloud and precipitation, temperature sounders are relatively insensitive to clouds, and provide important information about the atmosphere below. Initially microwave sounder observations were only used in 'clear-sky' conditions, but developments in model physics, assimilation techniques and radiative transfer codes led to the use of all-sky assimilation, where clear, cloudy or precipitating observations are assimilated using the same scattering-capable radiative transfer model (Geer *et al.*, 2017, and references therein). The all-sky approach is now used to assimilate microwave-sounding channels on the Special Sensor Microwave - Imager/Sounder (SSMIS; Geer, 2013; Baordo and Geer, 2016), Microwave Humidity Sounder (MHS; Geer *et al.*, 2014), GPM Microwave Imager (GMI; Lean *et al.*, 2017) and Micro-Wave Humidity Sounder-2 (MWHS-2; Lawrence *et al.*, 2018; Bormann *et al.*, 2021). At present, the humidity-sounding channels on the Advanced Technology Microwave Sounder (ATMS) instrument are still assimilated for clear-sky conditions only (e.g. observations affected by cloud and precipitation are screened out), though plans are to move towards all-sky assimilation of ATMS in the near-future. Figure 1 shows the global distribution of observations from instruments with microwave humidity sounding channels that are currently assimilated. Data are shown for one 30 minute period. The GMI swath width (∼900 km) is much narrower than for the other instruments (∼1700–2700 km) as the satellite orbits at a lower altitude due to the Dual-frequency Precipitation Radar.

Much of the benefit of assimilating humidity sounding channels comes from the 'tracer effect'. In the free-troposphere (e.g. away from the planetary boundary layer) the humidity field is primarily driven by winds. This allows the four-dimensional variational assimilation scheme (4D-Var) used at ECMWF to extract information about the atmospheric flow from humidity observations (Peubey and McNally, 2009). In the case of observations affected by cloud and precipitation, a more general 'model tracing' effect is seen (Geer *et al.*, 2014), which results from all of the physical processes that are modelled inside 4D-Var,

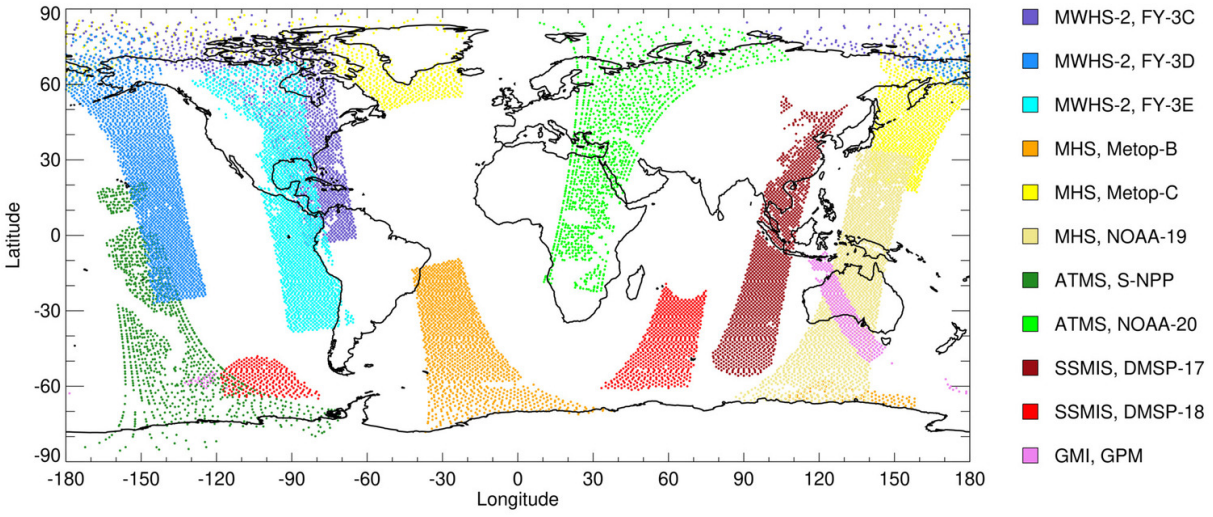

Figure 1: Global distribution of observations assimilated from cross-track and concial microwave scanners for one 30-minute time slot on 1 August 2023. Data from one humidity sounding channel on each instrument are shown.

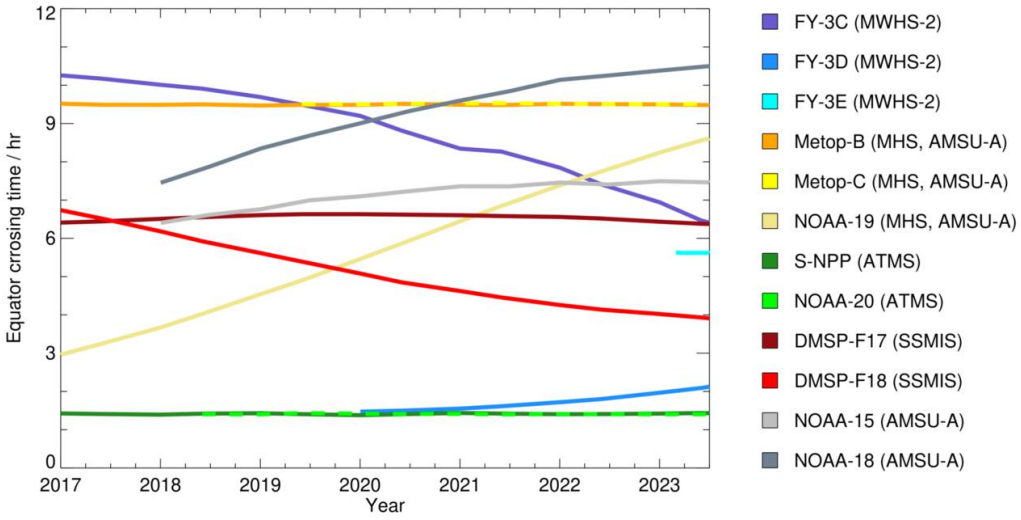

Figure 2: The variability of equator crossing times over the past 6.5 years from satellites carrying microwave sounder instruments.

such as large- and small-scale cloud formation and precipitation (Tompkins and Janisková, 2004; Lopez and Moreau, 2005). While observations from numerous microwave humidity and temperature sounders are currently assimilated, benefits are still seen when adding additional sounders into the assimilation, with saturation not yet reached (Duncan *et al.*, 2021).

The microwave humidity sounder observations currently assimilated are aboard satellites with a wide variety of equator crossing times (ECTs), as shown in Figure 2. The Coordination Group for Meteorological Satellites (CGMS) specifies a baseline for Low Earth Orbit satellites, which consists of coverage at 4-hour intervals, requiring three orbits at equally-spaced ECTs[1]. As seen in Figure 2, EUMETSAT's Metop satellites have a consistent ECT of 09:30, while NOAA's polar orbiting satellites have a consistent ECT of 13:30. The remaining satellites can be seen to drift much more in their ECT. To allow for the three-orbit baseline for NWP, the China Meteorological Administration (CMA) agreed to an early-morning orbit for their Fengyun-3E (FY-3E) satellite, with a 05:30 ECT (Zhang *et al.*, 2022). FY-3E is equipped with the same MWHS-2 instrument that was aboard FY-3C and FY-3D (see section 2 for further details).

Observations from microwave humidity sounders are thinned prior to assimilation for two reasons. Firstly, thinning helps to reduce the impact of spatially-correlated observation errors, which are not explicitly accounted for in 4D-Var. (The covariance matrix of observation errors, $\mathbf{R}$, is taken to be diagonal.) Secondly, thinning reduces the computing cost associated with large numbers of observations. However, the thinning scale for microwave humidity sounders has remained constant for many years, with a spacing of $\sim$111 km between observations. With increased computing power and the increasing resolution of ECMWF's forecasting model and 4D-Var scheme (for example the final analysis increments in operational forecasts are now calculated at 40 km resolution compared to 80 km when MW humidity sounders were first moved to all-sky assimilation), there is the potential to use data more densely, in order to extract additional information. A balance must be made though, as using observations too densely while neglecting spatial error correlations can result in a degraded analysis (Liu and Rabier, 2002, 2003; Stewart *et al.*, 2008; Hoffman, 2018).

[1] https://www.cgms-info.org/wp-content/uploads/2021/10/cgms-39-report.pdf

In this report we will address three questions on the subject of microwave humidity sounder assimilation at ECMWF:

1. Is there any benefit of adding data from the FY-3E MWHS-2 instrument to the current observing system?
2. Can we demonstrate that adding data from MWHS-2 in the early-morning orbit gives a greater forecasting impact than adding data close to an already-covered orbit?
3. What is the optimal spatial thinning scale for microwave humidity sounder observations?

These investigations into the NWP benefit of the early-morning orbiting FY-3E satellite and data thinning scales will help inform on how to extract the most benefit from both current and future microwave sounder instruments.

2 Overview of the MWHS-2 instrument

The MWHS-2 instrument has been flown on China's Fengyun-3 satellites, beginning with FY-3C in 2013, with FY-3D and FY-3E following in 2017 and 2021 respectively. MWHS-2 replaces the MWHS-1 instrument that was aboard FY-3A and FY-3B, which only had two 150 GHz channels and three 183 GHz channels. (FY-3B MWHS-1 data was operationally assimilated at ECMWF from 24 September 2014 to 1 June 2020; see Bormann *et al.*, 2021.) The FY-3C–E satellites are sun-synchronous polar-orbiting satellites, with current ECTs of 06:20, 02:10 and 05:35 (see Figure 2). MWHS-2 is a cross-track scanning instrument, with a swath width of 2700 km (the largest of any humidity sounder assimilated) and 98 fields of view (FOV). At nadir, the spatial resolution is 32 km for channels 1–9 and 16 km for channels 10–15, which is comparable to MHS and ATMS.

Information about the channels on MWHS-2 is given in Table 1. Like MHS, ATMS, SSMIS and GMI, MWHS-2 has channels centred on the strong water vapour absorption line at 183.31 GHz. There are also eight channels centred at the oxygen absorption line of 118.75 GHz. This is a frequency unique to MWHS-2, with the oxygen absorption band between 50–60 GHz instead used by instruments such as the Advanced Microwave Sounding Unit - A (AMSU-A) and ATMS for temperature sounding. The 183.31 GHz channels sample the atmosphere at different heights in the troposphere, while the 118.75 GHz channels sample the troposphere and stratosphere (Figure 3).

The 183.31 GHz channels are sensitive to water vapour, and also cloud and precipitation due to scattering from hydrometeors and absorption and emission by cloud liquid water (Geer *et al.*, 2017). As well as temperature, the 118.75 GHz channels are sensitive to clouds and precipitation in the lower peaking channels (5–7), and to humidity in channel 7 (di Michele and Bauer, 2006; Lawrence *et al.*, 2018). As the 118.75 GHz channels have relatively thin bandwidths, they have a higher noise equivalent delta temperature (NEdT). For example, taking channel 4 of MWHS-2 (118.75±0.3 GHz), the specified NEdT value is 1.6 K on FY-3C and FY-3D, and 0.8 K on FY-3E[2]. On AMSU-A channel 9 (which has a weighting function peak at a similar pressure level but is at a frequency of 57.29 GHz) the specified NEdT is 0.25 K[3]. The actual achieved NEdT is often lower than the specified value, and this is discussed further in section 3.3. As noted by Maddy *et al.* (2022), the performance gap between the 118 GHz and 50–60 GHz bands could be lessened by a reduction of instrument noise at 118 GHz. However, the 118 GHz band has

[2] http://www.nsmc.org.cn/nsmc/en/instrument/MWHS-2.html
[3] https://nwp-saf.eumetsat.int/site/software/aapp/aapp-overview/amsu-a

MWHS-2			Other instrument channel numbers			
Channel	Frequency (GHz)	Peak (hPa)	MHS	ATMS	SSMIS	GMI
1	89 (H)	Surface				
2	118.75±0.08 (V)	20				
3	118.75±0.2 (V)	60				
4	118.75±0.3 (V)	100				
5	118.75±0.8 (V)	250				
6	118.75±1.1 (V)	300				
7	118.75±2.5 (V)	700				
8	118.75±3.0 (V)	Surface				
9	118.75±5.0 (V)	Surface				
10	150 or 166 (H)	Surface				
11	183.31±1.0 (V)	350	3	22	11	
12	183.31±1.8 (V)	400		21		
13	183.31±3.0 (V)	500	4	20	10	12
14	183.31±4.5 (V)	550		19		
15	183.31±7.0 (V)	650	5	18	9	13

Table 1: MWHS-2 channel information, along with the channel numbers of other instruments that share the same frequencies. Rows highlighted blue show channels not assimilated. For channel 10, the frequency was 150 GHz on FY-3C and FY-3D, but changed to 166 GHz on FY-3E. The peak of the weighting functions are calculated at nadir for average clear-sky conditions (Lawrence et al., 2018)

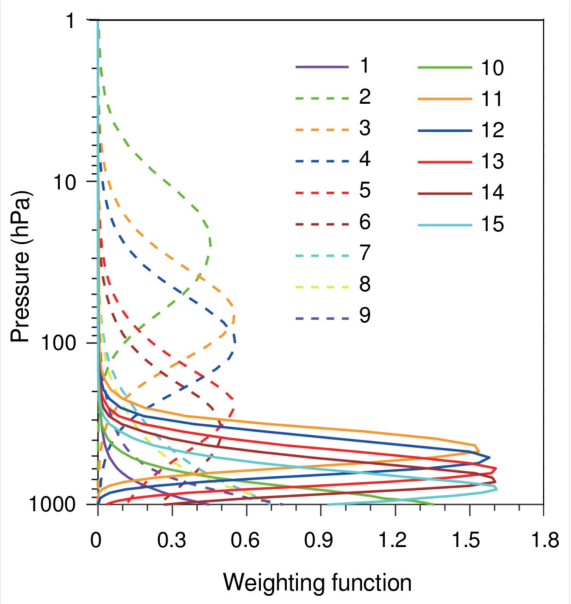

Figure 3: Weighting functions for the 15 MWHS-2 channels on board FY-3E (Mao et al., 2022).

a stronger sensitivity to ice clouds, and no reduction of instrument noise will be able to overcome this. Compared to MWHS-2 on FY-3C and FY-3D, the instrument on FY-3E has an almost twofold increase in sensitivity, and improved calibration accuracy (Mao *et al.*, 2022).

At ECMWF, the MWHS-2 instrument has been operationally assimilated since 4 April 2016 on FY-3C, and 2 December 2019 on FY-3D, and resulted in positive forecast impacts in the short-range, and neutral to slightly positive impacts in the medium range (Lawrence *et al.*, 2018; Duncan and Bormann, 2020). Of the 15 channels on MWHS-2, all five 183.31 GHz channels are assimilated, while six of the eight 118.75 GHz channels are assimilated (Table 1). Channels 8 and 9 are not assimilated as these have weighting function peaks at the surface, while channels 1 and 10 are window channels used for cloud detection in the all-sky observation error model (see section 3.2).

Assimilation of FY-3C and FY-3D MWHS-2 data has also been performed in other global forecast models (Jiang *et al.*, 2020; Carminati and Migliorini, 2021; Ma *et al.*, 2022), with larger improvements in short-range forecasts compared to medium-range forecasts. Ma *et al.* (2022) also assimilated the 118 GHz channels only, and noted they had a smaller impact than the equivalent AMSU-A channels. The newer FY-3E MWHS-2 data has been assimilated into the CMA global forecast model, and the impact was found to be similar to adding the ATMS instrument (Kan *et al.*, 2022), with larger improvements when assimilating the 118 GHz and 183 GHz channels together, rather than either in isolation (Xiao *et al.*, 2023). MWHS-2 data from FY-3C and FY-3D has also been used in regional models to study high-precipitation events in China (Liu *et al.*, 2021) and the forecast track and intensity of typhoons in the South China Sea (Xian *et al.*, 2019; Chen *et al.*, 2023), using the Weather Research and Forecasting model with 3D-Var. In these studies, assimilating MWHS-2 was found to improve forecasts, with better performance when assimilating data from FY-3C and FY-3D together, rather than either in isolation (Chen *et al.*, 2023).

3 Assimilating FY-3E MWHS-2 observations

3.1 Experimental setup

Two experiments were performed using ECMWFs Integrated Forecasting System (IFS). Both experiments make use of the full observing system, with the only difference being the addition of FY-3E MWHS-2 observations in one experiment. These observations are thinned to a spatial resolution of $\sim$111 km before being assimilated, to reduce the effects of spatially correlated observation errors. (The thinning scale is investigated in more detail in section 5.) The experiments were run from 11 October 2022 to 28 February 2023, but the first nine days are not included in any analysis to allow time for the variational bias correction scheme (VarBC; Auligné *et al.*, 2007) to spin up. For humidity sounders, VarBC consists of a global constant offset predictor, four predictors for air mass and three predictors for the scan angle.

IFS cycle 48R1 was used for the experiments, with 137 vertical levels and 12-hour long window delayed cutoff assimilation cycles. The model resolution was set to Tco399 (triangular-cubic-octahedral truncation at wavenumber 399), giving a grid spacing of $\sim$28 km. The assimilation scheme uses four inner loops of increasing resolution, with the final loop resolution being TL255 (triangular-linear truncation at wavenumber 255), which is $\sim$80 km. Background errors come from the operational ensemble of data assimilations (EDA) and thus represent a flow-dependent background error. For the radiative transfer calculations we used version 13 of RTTOV-SCATT (Radiative Transfer for TOVS microwave scattering package; see Bauer *et al.*, 2006; Geer *et al.*, 2017; Geer, 2021; Geer *et al.*, 2021; Geer *et al.*, 2022).

3.2 Observation error modelling

As the IFS cannot precisely forecast the location and intensity of clouds and precipitation, the dominant source of random error in cloudy and precipitating situations is representivity, not instrument noise or radiative transfer inaccuracies (Geer and Bauer, 2011). For operational assimilation, these representivity errors are treated as observation errors, and as such an appropriate observation error model is required. Here we use the error model of Geer and Bauer (2011), which was originally developed for use with all-sky microwave imager radiances. In this model, observation errors are increased as a function of a symmetric cloud amount, C_{sym}, which is calculated from a scattering index (SI). For observations over land, the difference between brightness temperatures (TB) in the channels closest to 90 GHz and 150 GHz are used to calculate the SI:

$$\text{SI}_{\text{land,obs}} = \text{TB}_{90} - \text{TB}_{150}. \tag{1}$$

For MWHS-2, this corresponds to channels 1 and 10 respectively (see Table 1). As the effects of scattering are greater at 150 GHz than at 90 GHz, the 150 GHz brightness temperatures are suppressed in scattering cloud situations, giving a positive SI. An SI of ~50 K is typically associated with deep convection (Geer *et al.*, 2014). Over oceans, water vapour absorption can cause large differences between TB_{90} and TB_{150}, and so a clear-sky term (calculated from the model first guess) is subtracted, which removes the effect of water vapour absorption:

$$\text{SI}_{\text{ocean,obs}} = (\text{TB}_{90} - \text{TB}_{150}) - (\text{TB}_{90}^{\text{clr}} - \text{TB}_{150}^{\text{clr}}). \tag{2}$$

Scattering indices over land and ocean are also calculated in the same way from the IFS brightness temperatures that have been bias-corrected ($\text{SI}_{\text{land,ifs}}$, $\text{SI}_{\text{ocean,ifs}}$), and these are combined to give symmetric cloud predictors:

$$C_{\text{sym,land}} = (\text{SI}_{\text{land,obs}} + \text{SI}_{\text{land,ifs}})/2 \tag{3}$$

$$C_{\text{sym,ocean}} = (\text{SI}_{\text{ocean,obs}} + \text{SI}_{\text{ocean,ifs}})/2 \tag{4}$$

The calculated C_{sym} values (over land or ocean) are then used in conjunction with specified clear and cloudy values (C_{clr}, C_{cld}) to determine the observation error, g:

$$g(C_{\text{sym}}) = \begin{cases} g_{\text{clr}} & C_{\text{sym}} \leq C_{\text{clr}} \\ g_{\text{clr}} + (g_{\text{cld}} - g_{\text{clr}}) \left(\frac{C_{\text{sym}} - C_{\text{clr}}}{C_{\text{cld}} - C_{\text{clr}}} \right)^2 & C_{\text{clr}} < C_{\text{sym}} < C_{\text{cld}} \\ g_{\text{cld}} & C_{\text{sym}} \geq C_{\text{cld}} \end{cases} \tag{5}$$

Table 2 gives the values used in the observation error model for the assimilated channels, which are based on O–B statistics (Geer and Bauer, 2011). Here, O is the observed value and B is the equivalent value from the model forecast (also known as the 'background'). The value of B is obtained through spatial interpolation from model space to observation space, followed by a radiative transfer calculation using RTTOV-SCATT. The observation errors for the 118 GHz channels are lower for FY-3E than FY-3C or FY-3D due to the lower instrument noise. Channels 2–4 peak too high in the atmosphere to be sensitive to cloud amount (see Figure 3), so constant observation errors are used. Figure 4 shows examples of the standard deviation of O–B (black lines) from FY-3E MWHS-2 as a function of C_{sym} for two channels (one temperature-sounding and one humidity-sounding) over ocean and land. The dashed pink line shows the corresponding observation errors from Equation 5. As can be seen, the error model begins to deviate from the standard deviation of O–B for larger C_{sym} values. However, as shown by the green line, the number of observations for large C_{sym} is low, and it is more important for the error model to fit the bulk

	Land				Ocean			
Channel	g_{clr}	g_{cld}	C_{clr}	C_{cld}	g_{clr}	g_{cld}	C_{clr}	C_{cld}
2	2	2	0	0	2	2	0	0
3	1	1	0	0	1	1	0	0
4	0.8	0.8	0	0	0.8	0.8	0	0
5	0.8	5	3	30	0.8	2.2	3	45
6	0.8	10	0	35	0.8	5	0	40
7	1.5	22	0	30	1.5	16	0	40
11	2.2	40	-2	55	2	12	0	55
12	2.2	50	-2	40	2	15	0	50
13	2.2	58	0	35	2	18	0	40
14	2.2	68	0	30	2	20	0	45
15	2.2	75	0	30	2	27	0	40

Table 2: Parameters of the observation error model over land and ocean for FY-3E MWHS-2 (see equation 5). All values are in Kelvin, and are given for assimilated channels only.

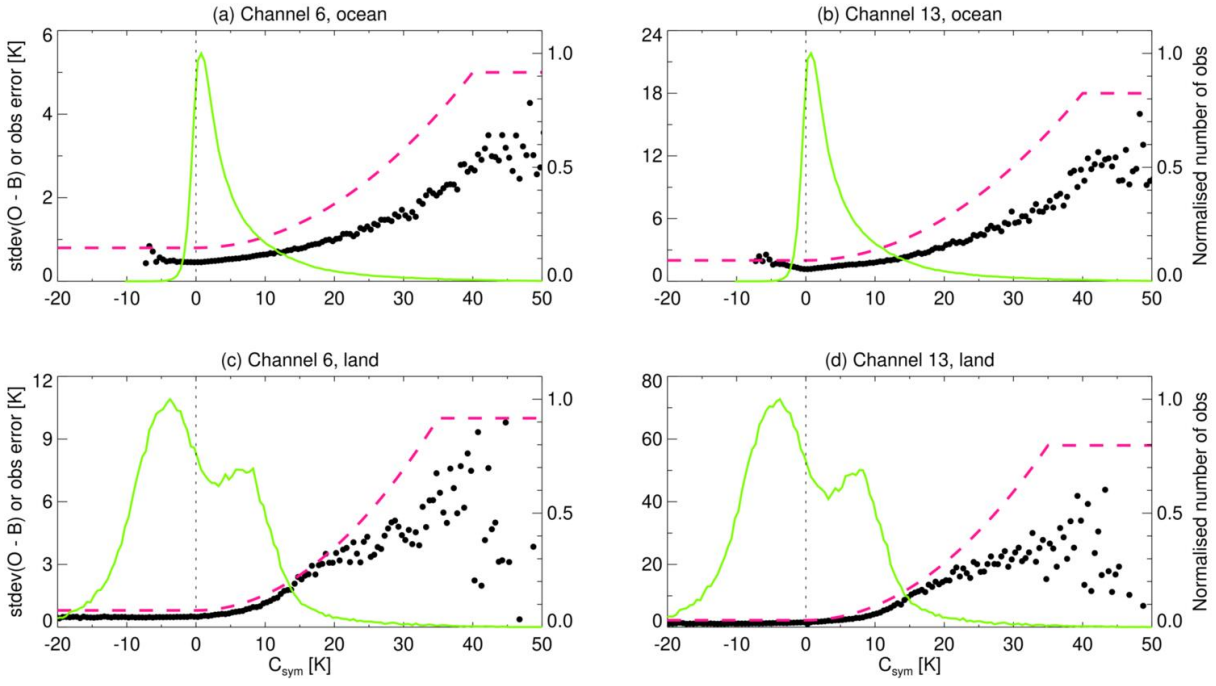

Figure 4: Standard deviation of first-guess departures from FY-3E MWHS-2 as a function of the symmetric cloud predictor (black dots) along with the applied observation error (pink dashed line) and the normalised number of observations in each bin (green line). Values are shown for channels 6 and 13, over ocean and land. Based on data from February 2023, with a C_{sym} bin size of 0.5 K.

of the observations, which are found at lower C_{sym} values. Additionally, further tuning of the error model can be undertaken once observations have been assimilated for a longer period of time, giving a larger dataset from which to calculate statistics.

3.3 Assessing the data quality

Before investigating the impact of assimilating FY-3E MWHS-2 data, we first assess the data quality and compare it to other similar instruments. To do this we use data from February 2023 and compute O–B statistics. We only use observations if they match the following criteria:

1. The observation is over ice-free oceans.
2. The observation and model SI are less than 5 K.
3. The instrument zenith angle is less than 60°.
4. The abs(latitude) value is less than 60°.

These selection criteria ensure we only use 'clear-sky' data over oceans (so the results are not impacted by incorrect modelling of clouds or surface properties) and we avoid potential issues with observations at the outer scan positions of each swath (discussed in more detail later). We then calculate the O–B mean and standard deviation. Note that the SI calculation for determining cloud contamination uses the difference between MWHS-2 channels 1 and 10 (Table 1). For FY-3E the frequency of channel 10 was increased from 150 GHz to 166 GHz, making it slightly more sensitive to cirrus clouds. As such, there is likely to be less cirrus contamination in the FY-3E O–B statistics.

Figure 5 shows the standard deviation and mean of O–B for the assimilated temperature and humidity channels, which reveals information about instrument noise and observation biases respectively. Results are shown for MWHS-2 on FY-3C, FY-3D and FY-3E before bias correction (solid lines) and after bias correction (dashed lines). Comparisons are made against the MHS instrument (see Table 1) for the humidity channels (11–15), and AMSU-A for the temperature channels (2–7). As AMSU-A samples the 50-60 GHz band, compared to 118 GHz for MWHS-2, direct comparison cannot be made between channels. Instead, we compare channels with weighting functions that peak at similar pressure levels (see Table 3 of Lawrence *et al.*, 2015). The two most important results from Figure 5a are as follows:

1. For the temperature channels, FY-3E shows a clear improvement in noise, being typically 0.2–0.3 K lower than FY-3D. (See also Table 3.) This lower noise is also clear in maps of O–B as shown in Figure 6(a,c). Compared with AMSU-A, the noise in MWHS-2 is consistently larger. This is in agreement with the results of Kan *et al.* (2022).
2. For the humidity channels it can be seen that the noise is almost identical between FY-3E and FY-3D (both of which have lower noise than FY-3C) and compares well with similar channels on MHS. This similarity can also be seen in maps of O–B for one day, shown in Figure 6(b,d), though note that these maps show all observations rather than cloud-free observations over ocean that were used to make Figure 5.

In terms of biases (Figure 5b), FY-3E has a consistent negative bias, whereas FY-3C and FY-3D have varying positive and negative biases. Compared to MHS and AMSU-A, the magnitudes of the FY-3E biases are larger, with the exception being channel 11. After bias correction the mean O–Bs are

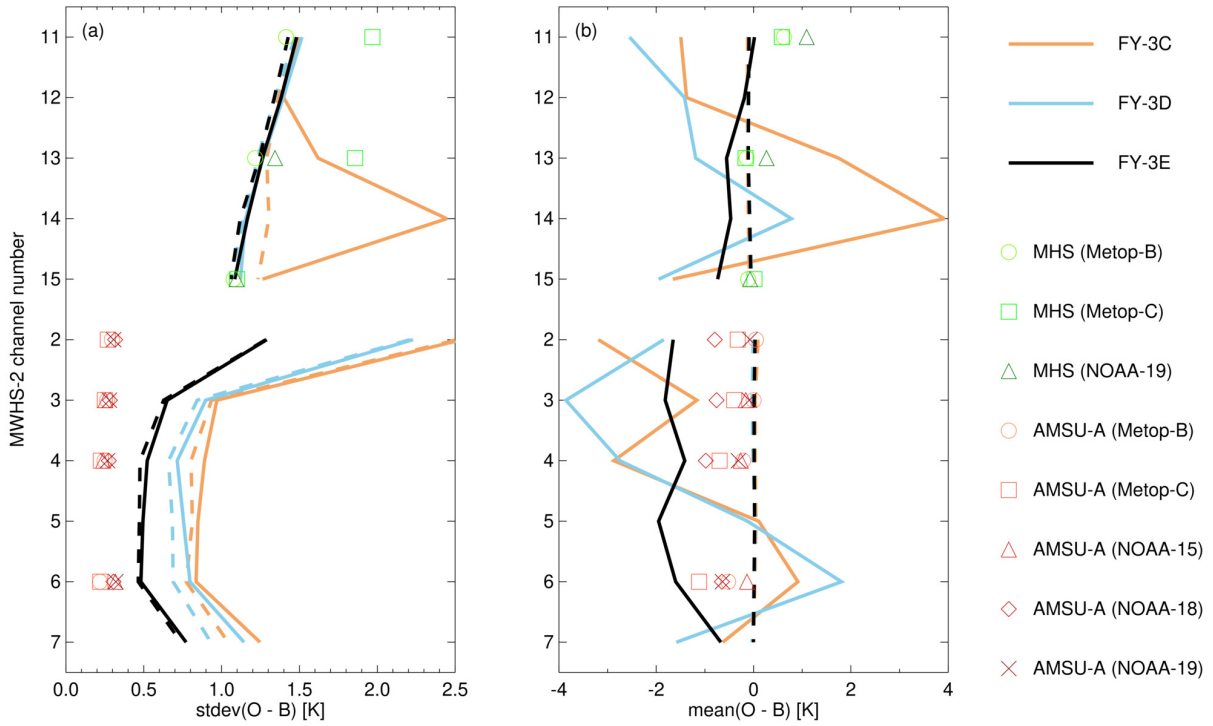

Figure 5: Background departure statistics for assimilated channels of MWHS-2 on FY-3C, FY-3D and FY-3E. The (a) standard deviation of O–B, and (b) mean O–B, are calculated from data covering 1–28 February 2023. Solid and dashed lines show values before and after bias correction. Only clear-sky data are used (cloud-free observations over ice-free oceans; see text for further details). Coloured symbols show comparisons against similar channels on other instruments before bias correction.

	Specified NEdT			Achieved NEdT		
Channel	FY-3C	FY-3D	FY-3E	FY-3C	FY-3D	FY-3E
2	3.6	3.6	2.2	2.5	2.2	1.3
3	2.0	2.0	1.0	1.0	0.9	0.7
4	1.6	1.6	0.8	0.9	0.7	0.5
5	1.6	1.6	0.8	0.8	0.8	0.5
6	1.6	1.6	0.8	0.8	0.8	0.5
7	1.6	1.6	0.8	1.2	1.1	0.8

Table 3: The specified MWHS-2 NEdT values for the assimilated temperature channels, along with the achieved values, which are determined from the standard deviation of clear-sky O–B departures shown in Figure 5. All values are in Kelvin.

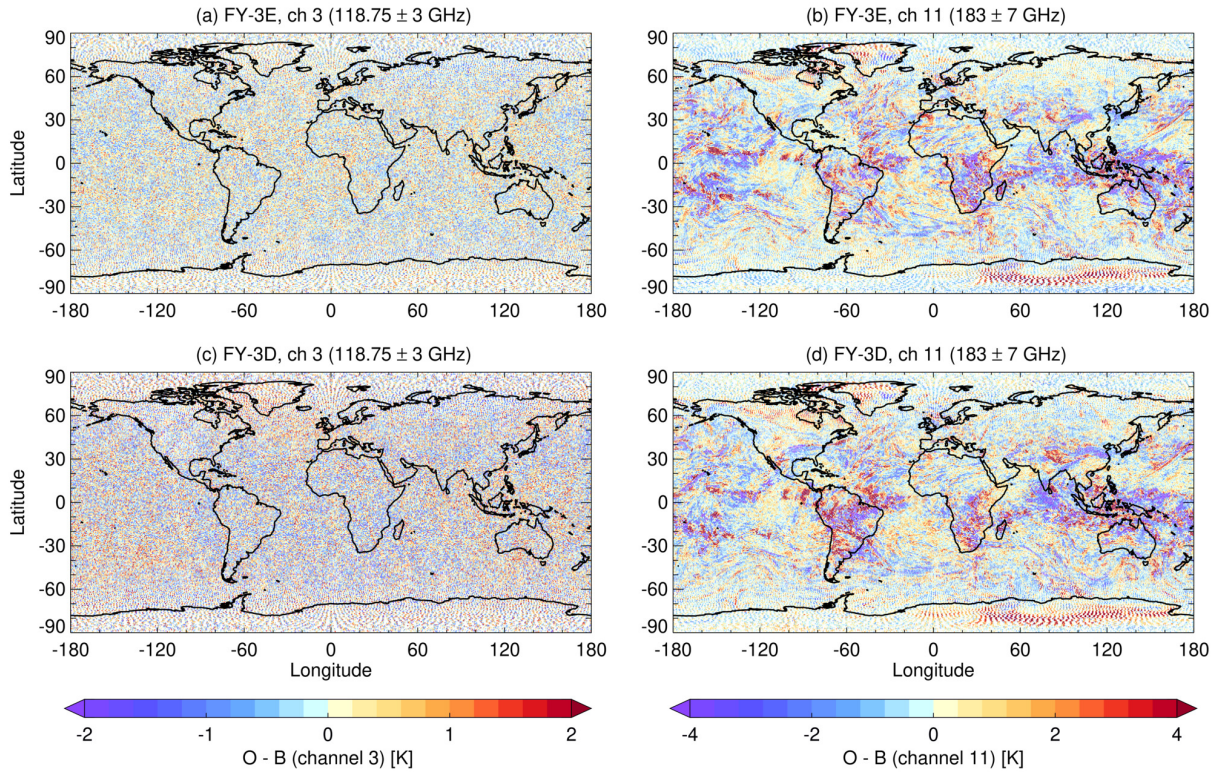

Figure 6: Maps of O–B for channels 3 (temperature sounding) and 11 (humidity-sounding) from 1 February 2023. Data are shown for (a,b) FY-3E and (c,d) FY-3D.

similar for all three FY-3 satellites, and all close to zero. Figure 7 shows a more detailed view of the MWHS-2 biases before bias correction has been applied, displaying normalised histograms of O–B. The histograms on FY-3E follow a Gaussian distribution (which is good as this is what 4D-Var assumes), and typically have taller peaks and reduced spread compared to FY-3C and FY-3D, indicating a lower noise (particularly noticeable for the temperature channels 2–7). The similarity between the histogram shapes of the humidity channels (11–15) on FY-3D and FY-3E shows how similar the MWHS-2 noise is between these two satellites.

Finally, Figure 8 shows MWHS-2 biases as a function of the scan position, where MWHS-2 has 98 scan positions with the zenith angle extending to around $\pm 66°$. For the water vapour channels (11–15), MWHS-2 on FY-3E has a bias closer to zero compared to FY-3C and FY-3D. For the temperature channels (2–7) there is more channel-to-channel variability in the bias, with FY-3E sometimes having a larger or smaller absolute bias compared to FY-3C and FY-3D. Also noticeable are the larger biases seen in the outer two scan positions (1, 2 and 97, 98). For this reason, these scan positions are excluded from assimilation. While it is useful to compare the scan biases before bias correction has been applied, what is more important are the scan biases after the VarBC procedure. These are shown for FY-3E by the green line in Figure 8. It can be seen that in general VarBC handles the scan position biases well, reducing them to almost straight lines around the zero value. The main outlier is channel 7, where the cubic polynomial used by VarBC has difficulty to correct the 'm-shaped' bias. This is also true for channel 7 on FY-3C (not shown) which also has a similar 'm-shaped' bias, whereas VarBC better handles channel 7 of FY-3D, despite it having a larger bias. Even considering this small issue with channel 7, the results presented here suggest that FY-3E MWHS-2 has a data quality suitable for assimilation.

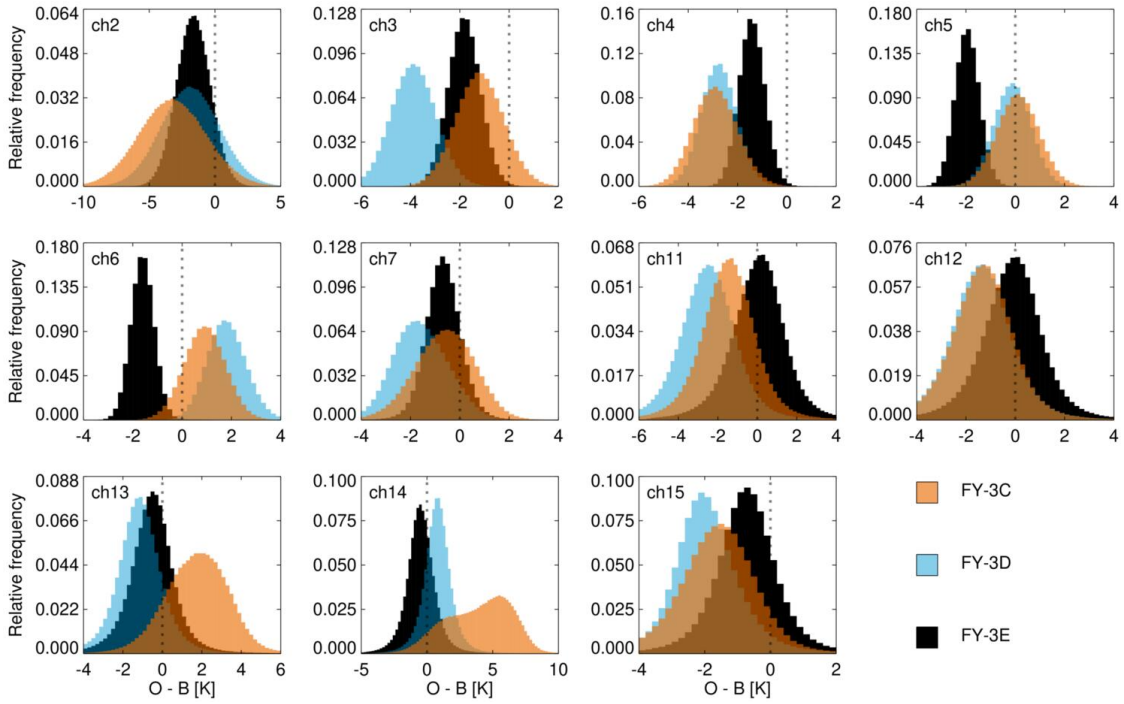

Figure 7: Histograms of O–B (before bias correction) for the assimilated channels of MWHS-2 on FY-3C, FY-3D and FY-3E. Calculated from clear-sky data covering 1–28 February 2023.

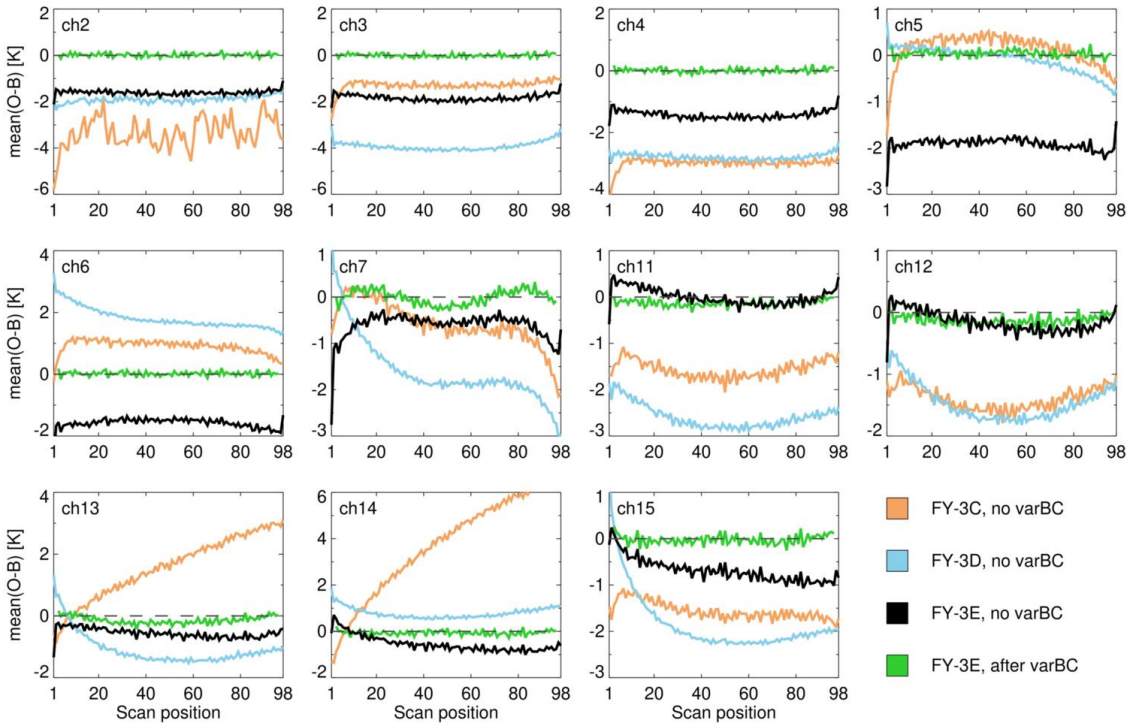

Figure 8: Mean O–B as a function of scan position for the assimilated channels of MWHS-2 on FY-3C, FY-3D and FY-3E. Calculated from clear-sky data covering 1–28 February 2023.

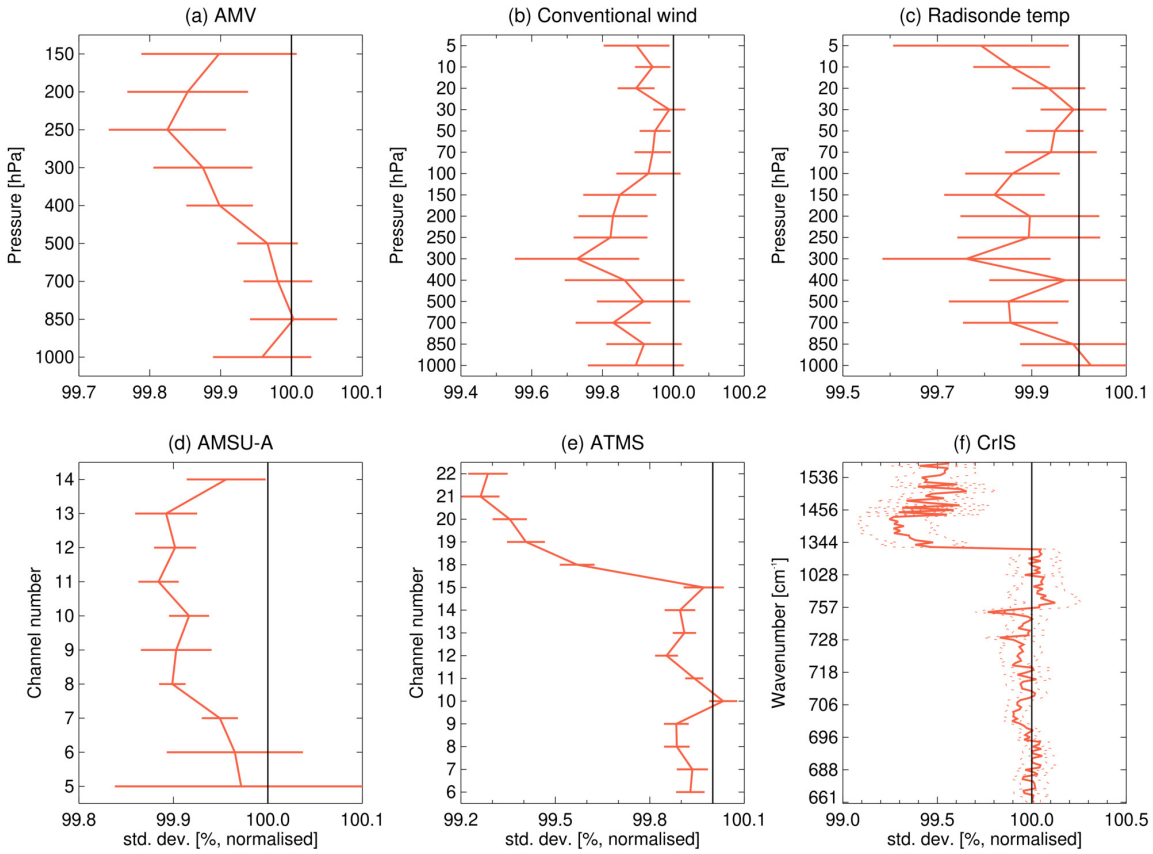

Figure 9: Standard deviation of O–B from an experiment assimilating FY-3E MWHS-2 data (red line), normalised by a control experiment with no FY-3E data assimilated (black line). Each panel shows comparisons against a different observation type, and verification is against the operational ECMWF analysis covering 20 October 2022 to 28 February 2023. The 95% confidence range (see Geer, 2016) is represented by (a–e) horizontal red lines, and (f) dashed lines for clarity, due to the large number of channels.

3.4 Impact on short- and medium-range forecasts

In this section we investigate the impact of assimilating FY-3E MWHS-2 data, using the setup described in section 3.1. We begin by looking at the impact on short-range 12 hour forecasts. Figure 9 shows the O–B standard deviation from an experiment assimilating FY-3E MWHS-2 data, normalised by the O–B standard deviation of a control experiment which excludes FY-3E MWHS-2 data, expressed as a percentage ($100 \cdot \sigma_{\mathrm{MWHS2}} / \sigma_{\mathrm{control}}$). These statistics were compiled from 263 individual 12 hour forecasts. Values less than 100% represent an improvement to the short-range forecast when assimilating FY-3E MWHS-2 data, while values greater than 100% represent a forecast degradation. Such statistics are calculated against all assimilated instruments, but Figure 9 shows comparisons against six instruments, representing a range of different data types.

Figure 9(a,b) shows comparisons against different types of wind observations: atmospheric motion vectors (AMVs), which are derived from tracking cloud or water vapour features from satellite data, and conventional wind observations (aircraft, radiosondes and radar profilers) respectively. As can be seen from both panels, the biggest improvement to the winds occurs around the 250–300 hPa range, though the improvement is only small at ∼0.15–0.2%, but statistically significant. At this pressure range AMVs and conventional wind observations have large numbers of observations, with the number dropping rapidly

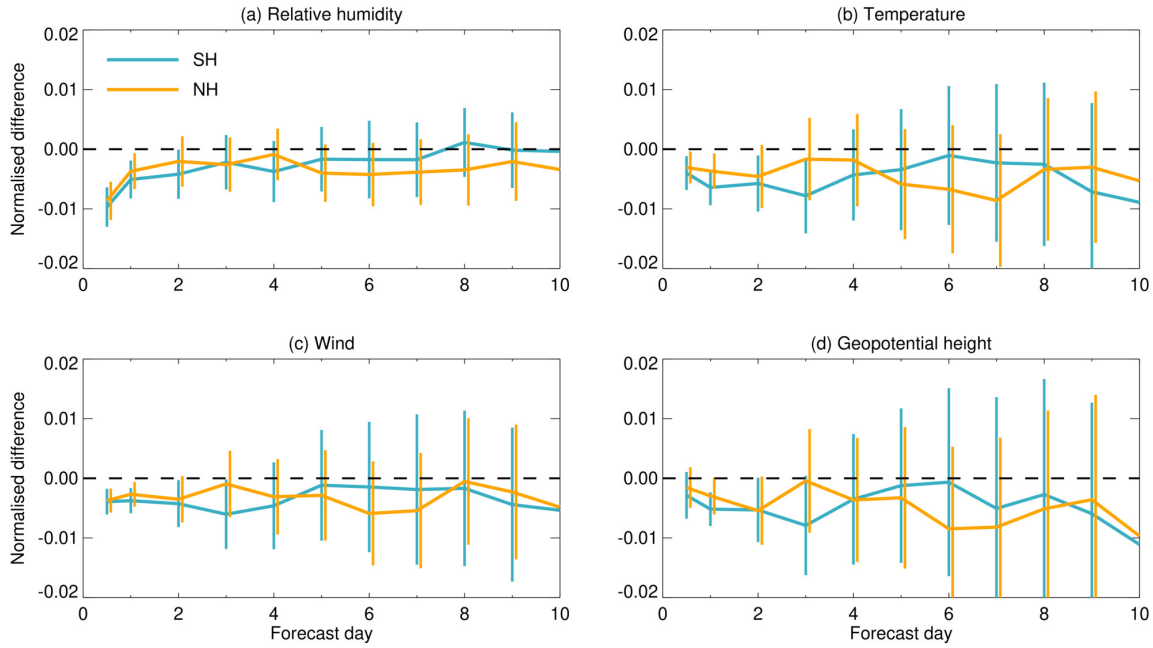

Figure 10: Normalised change in RMS error (when comparing the FY-3E MWHS-2 assimilation against the control) for four different parameters at 500 hPa across a 10 day forecast. Blue and orange lines show results for the southern and northern hemispheres respectively. Vertical lines show the 95% confidence range. Verification is against the operational ECMWF analysis, covering the full four months of experimentation.

at higher altitudes (e.g. for conventional winds there are ∼35 million observations at 250 hPa, but only ∼4 million at 150 hPa). For radiosonde temperatures (Figure 9c), the general signal is towards improvements when assimilating FY-3E MWHS-2, though there are much fewer radiosonde observations (around 8 times fewer than conventional wind observations) and they are limited in their global coverage. A better impact on temperature can be determined from satellite instruments with global coverage. Figure 9(d–f) shows comparisons against the Advanced Microwave Sounding Unit - A (AMSU-A), ATMS and the Cross-track Infrared Sounder (CrIS), all of which have temperature-sounding channels. There is a small but statistically-significant improvement to temperatures in AMSU-A and in the temperature-sounding channels of ATMS (channels 6–15), while there is a more neutral impact to CrIS temperature channels (wavenumbers up to ∼757 cm^{-1}). The largest impact from assimilating FY-3E MWHS-2 data can be seen in the humidity-sensitive channels (18–22 on ATMS, and wavenumbers above ∼1344 cm^{-1} on CrIS), where the improvement is up to ∼0.7%. The behaviour shown in Figure 9 is similar for the other instruments not shown, with slight improvements when comparing against temperature and wind observations, and greater improvements when comparing against humidity-sensitive observations.

In terms of medium-range impact, Figure 10 shows the normalised change in RMS error, ε, when comparing the assimilation of FY-3E MWHS-2 data against the control; $(\varepsilon_{\text{MWHS2}} - \varepsilon_{\text{control}})/\varepsilon_{\text{control}}$. In this case, the errors are calculated by comparing the assimilation and the control experiments against the operational ECMWF analysis, rather than comparing against individual instruments. Results are shown for four different model parameters at 500 hPa, and are split into northern and southern hemisphere extra-tropics. For statistically-significant changes, improvements can be seen out to day 3, and possibly day 4. This is most notable for the southern hemisphere, where temperature, wind and geopotential height are improved by ∼0.6–0.8% at day 3. The fact that the biggest improvement is seen in the southern hemisphere has also been noted in other experiments assimilating MWHS-2 data from FY-3C/FY-3D into the IFS (Lawrence *et al.*, 2018; Duncan and Bormann, 2020), FY-3D (Duncan and Bormann, 2020), and

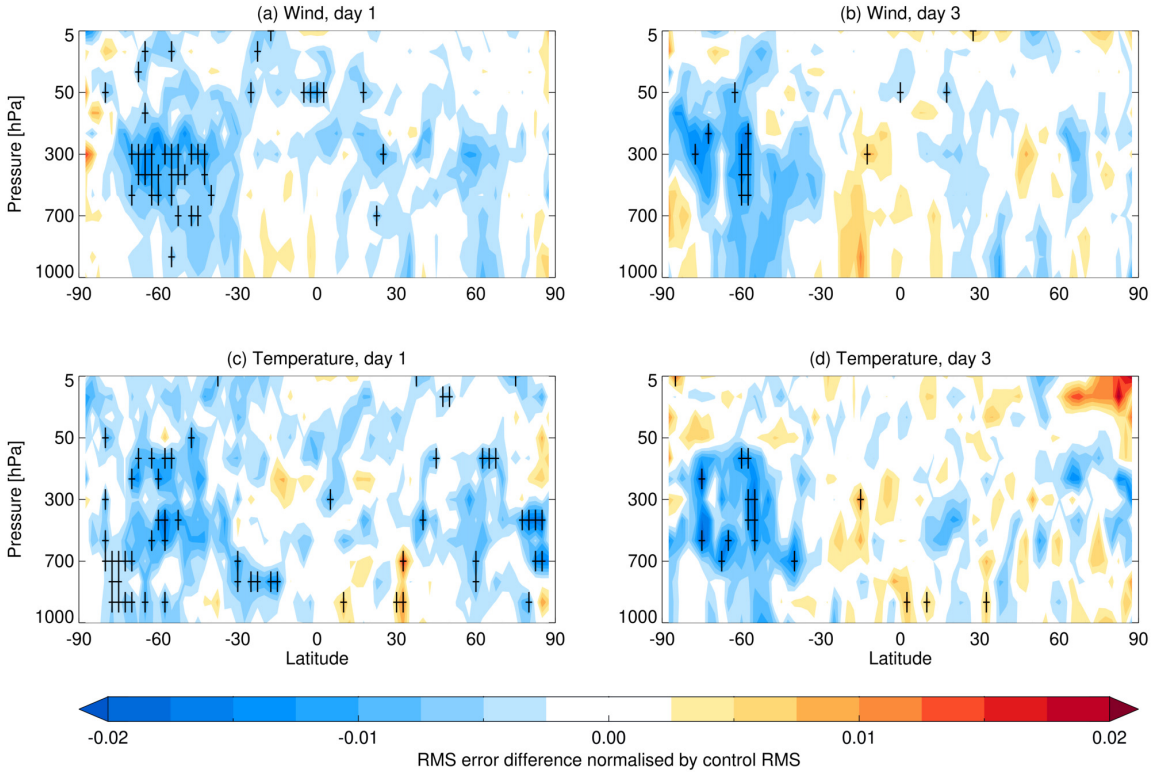

Figure 11: Normalised difference in RMS error (when comparing the FY-3E MWHS-2 assimilation against the control) as a function of latitude and pressure for wind and temperature at forecast days 1 and 3. Cross-hatching indicates the 95% confidence level. Verification is against the operational ECMWF analysis, covering the full four months of experimentation.

assimilating FY-3E MWHS-2 data into the Chinese Meteorology Administration global forecast system (Kan *et al.*, 2022).

Figure 11 shows the results for forecast days 1 and 3 in more detail, where now the zonal averages of wind and temperature are shown, allowing the effects on different pressure levels to be seen. Blue/red colours highlight regions with forecast improvements/degradations respectively, with black cross-hatching signifying statistically-significant changes. Similar to Figure 10, the largest improvements can be seen in the southern hemisphere, with statistically-significant improvements between ∼50–700 hPa. The results are more neutral in the tropics and northern hemisphere by day 3, with some improvements seen in the troposphere, and some degradations in the stratosphere above the north pole, but neither being statistically significant.

Because of the results of the data quality and assimilation experiments, it was decided to include FY-3E MWHS-2 in the ECMWF operational forecast. The sensor became active on 22 February 2023.

4 Does the FY-3E orbit contribute to forecast improvement?

The previous section showed how short- and medium-range forecast improvements were seen in the experiment assimilating FY-3E MWHS-2 data. As noted in section 1, FY-3E has an early-morning orbit (with an equator-crossing time, ECT, of 05:30), which complements the orbits of EUMETSAT's Metop

satellites (09:30 ECT), and NOAA's polar-orbiting satellites (13:30 ECT). In this section we investigate the difference in NWP impact if (1) we add data from an orbit that optimally complements other already-committed orbits in terms of ECT, or (2) we add data from an orbit that is already well-covered in terms of ECT. Eyre and Weston (2014) showed from a set of simplified experiments that polar orbiting satellites should be equally-spaced in time to obtain the biggest improvement to NWP, but the results depend on the growth of the forecast error variance. This agrees with the results of di Tomaso and Bormann (2011) who showed that three microwave sounders in complementary orbits (ECTs of 09:30, 13:41 and 16:50) gave a better forecast impact than those with non-complementary orbits (ECTs of 09:30, 13:41 and 13:58).

4.1 Experimental setup

We use the same general experimental setup as detailed in section 3.1, with the only difference being the observations assimilated. As shown in Figure 2, we are currently in a 'lucky period', with many heritage instruments performing beyond their specified lifetimes. This results in a large variety of ECTs, but this situation will not last forever. To assess the impact of the complementary orbit of FY-3E we therefore remove any microwave instruments from the assimilation that are aboard satellites not in the 09:30 or 13:30 orbits specified by the CGMS. This leaves only the Metop-B and Metop-C satellites at 09:30 ECT (containing MHS and AMSU-A) and the S-NPP and NOAA-20 satellites at 13:30 ECT (containing ATMS). Using this reduced observing system we perform three experiments:

1. A 'control' which contains no MWHS-2 data.
2. An assimilation of FY-3D MWHS-2 data. These have an ECT of 02:00, which is close to the 1:30 orbit already covered by ATMS data in these experiments.
3. An assimilation of FY-3E MWHS-2 data. These have an ECT of 05:40, which is complementary to the other ECTs in these experiments.

Comparing experiments 2 and 3 against experiment 1 will show to what extent adding data in a complementary orbit provides more impact than adding data into the already-covered afternoon orbit. As the 118 GHz temperature-sounding channels on MWHS-2 have different noise values for FY-3D and FY-3E, they are excluded from the assimilation and only the humidity-channels are added in experiment 2 and 3. Both MWHS-2 instruments hence are considererd of similar data quality, and they are treated consistently in both experiments.

4.2 Impact on short- and medium-range forecasts

To begin with, we look at the impact on short-range 12 hour forecasts by comparing against other observations. Figure 12 shows the O–B standard deviations from the experiments assimilating FY-3D data (blue line) and FY-3E data (red line) normalised by the O–B standard deviation of the control experiment. Comparisons are shown against instruments sensitive to humidity and wind; temperature-sensitive observations display little difference so are not shown here.

Figure 12a shows comparisons against water vapour channels on five different geostationary satellites: Meteosat 9 and 11, Himawari 8, and GOES 16 and 17. It is clear that assimilating MWHS-2 data from either FY-3D or FY-3E improves the match with the observations, but there is a much larger impact when assimilating data from FY-3E. The impact is largest for Metop 11 and Himawari 8, where there is a

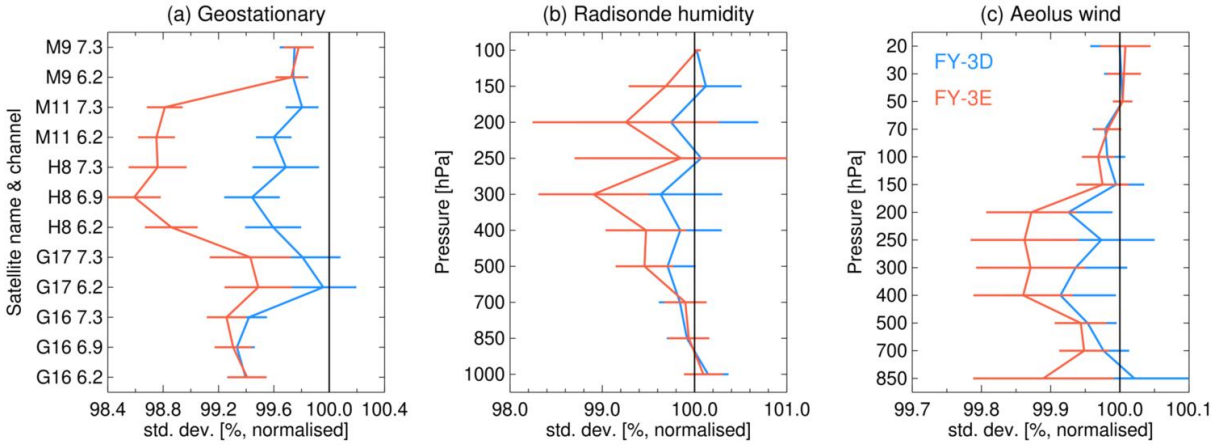

Figure 12: As Figure 9, but from experiments assimilating MWHS-2 data from FY-3D (blue line) and FY-3E (red line), normalised by a control experiment (black line; see text for details). For geostationary data the instruments are Meteosat 9 and 11 SEVIRI (M9, M11), Himawari 8 AHI (H8) and GOES 16 and 17 ABI (G16, G17), with water vapour bands at 6.2, 6.9 and 7.3 microns. Aeolus observations are Rayleigh clear winds. Statistics are compiled from global data covering 20 October 2022 to 28 February 2023, apart from Himawari 8 and GOES 17, which stopped being assimilated on 12 December 2022 and 4 January 2023, respectively.

$\sim$1.2% improvement to the forecast, while there is little difference between assimilating FY-3D and FY-3E data for Meteosat 9 and GOES 16. This difference is likely due to the times when the FY-3 satellites overpass the geostationary satellite regions. For example, for Meteosat 11 and Himawari 8 the FY-3E overpass is at the end of the assimilation window. This means that for the subsequent assimilation cycle the Meteosat 11 and Himawari 8 areas have benefited from the FY-3E data most recently, leading to larger improvements in O–B over this area, as seen in Figure 12a. For GOES 16, GOES 17 and Meteosat 9 the FY-3E overpass is towards the start or middle of the assimilation window, and hence smaller improvements to the O–B are seen. The same holds true for FY-3D. For GOES 16 and Himawari 8 the overpass is at the end of the assimilation window, and these show larger improvements in Figure 12a. The smallest improvements are seen for Meteosat 9 and GOES 17, for which the FY-3D overpass is at the beginning of the assimilation window. The fact that there is no geostationary satellite for which FY-3D performs better than FY-3E suggests there is less benefit to adding a satellite into an already-covered orbit (the FY-3D orbit is covered by S-NPP and NOAA-20).

A comparison against radiosonde humidity observations is shown in Figure 12b. Lower in the troposphere the impact from FY-3D and FY-3E is similar, but FY-3E shows a larger impact higher in the troposphere, between around 200–700 hPa. Due to the limited number of radiosonde observations, and limited global coverage, the statistical significance is lower than for the geostationary satellites. Aeolus Rayleigh clear wind observations are shown in Figure 12c, and extend into the stratosphere. For the troposphere, FY-3E data shows a bigger improvement to the forecast winds than FY-3D, and the improvement extends to higher altitudes than the highest-peaking channel assimilated (channel 11, with a peak at $\sim$350 hPa; see Figure 3). Little impact is seen for stratospheric winds, which may be due to the assimilation only including tropospheric water vapour channels. Additionally, the number of Aeolus observations drops off rapidly at altitudes above $\sim$100 hPa, giving a smaller data set from which to calculate robust statistics.

In terms of medium-range impact, Figure 13 shows the normalised difference in RMS error for wind, as a function of latitude and pressure, at forecast days 1–3. Results are shown for the assimilation of humidity

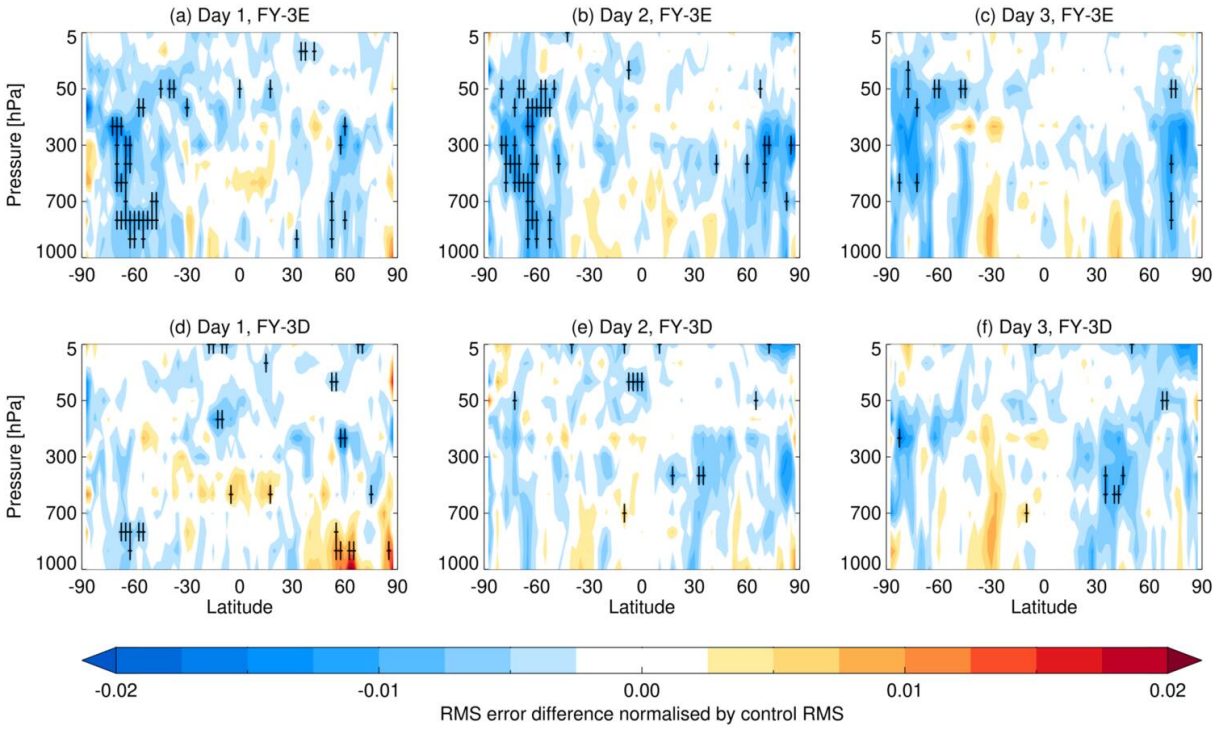

Figure 13: As Figure 11, but only showing results for wind at forecast days 1–3 from experiments assimilating MWHS-2 data from (a–c) FY-3E, and (d–f) FY-3D.

channels from FY-3E (Figure 13a–c) and FY-3D (Figure 13d–f). The errors are calculated by comparing the forecasts from the assimilation and the control experiments against the operational ECMWF analysis. Statistically-significant changes are shown with black hatching. Only wind is shown, as the assimilation of humidity channels has little impact on temperature and geopotential. It is clear that assimilation of FY-3E data results in a larger improvement out to day 3, particularly in the southern hemisphere (with improvements of $\sim$1.5%) but also in the northern hemisphere too.

As has been shown, there is clear evidence that adding data from an instrument with a complementary ECT (in this case FY-3E MWHS-2 with an ECT of 05:40) provides beneficial impacts compared to adding data from an instrument with identical noise in an already well covered orbit in terms of ECT. When performing the same experiments with an assimilation system including all drifting satellites (see Figure 2), the impact of the complementary 05:40 orbit is much less obvious. However, as noted earlier, these heritage instruments on satellites with drifting orbits are not guaranteed to continue operating. Thus, the three-orbit constellation, as specified by the Coordination Group for Meteorological Satellites should be maintained in order to provide the most benefit to NWP.

5 Assessing the thinning scale for humidity sounder observations

The previous two sections investigated the impact of assimilating data from microwave humidity sounders. However, not all data supplied are used for assimilation. Instead, the data are thinned or superobbed (where multiple observations are averaged into one ‘super observation’ with reduced noise), which (1) reduces the computing cost associated with large numbers of observations, and (2) reduces the problem

of spatially-correlated errors which are not accounted for in the 4D-Var assimilation scheme. Indeed, using observations too densely while neglecting spatial error correlations can result in degraded forecasts (Liu and Rabier, 2002, 2003).

In this section, we investigate the thinning scale used for all-sky microwave humidity sounders (MHS and MWHS-2) to see if any improvement to the forecast can be made through increasing the amount of data assimilated. This is motivated by the fact that the resolution of the IFS has increased significantly since the presently-used thinning scale of 111 km was chosen. It is possible that in different regions of the atmosphere different thinning scales may be appropriate, such as smaller scales in regions with sharp gradients (Dando *et al.*, 2007), which could be addressed with adaptive thinning (e.g. Ochotta *et al.*, 2005; Hoffman, 2018; Kim *et al.*, 2020; Mallick, 2022). Duncan *et al.* (2023) experimented with finer thinning scales for all-sky humidity sounders (down to 80 km observation spacing), and also a combination of finer thinning and superobbing (down to 70 km spacing). The results showed that superobbing reduced sensor noise (particularly for the 118 GHz channels of MWHS-2), with the combination of 50 km superobs and 70 km thinning providing the best results. These experiments were performed with the IFS at Tco399 ($\sim$28 km) resolution. Here we do not consider superobbing, but instead we are interested in to what degree the thinning scale is dependent on the model resolution. As such we perform experiments at two different model resolutions, and explore more thinning scales than Duncan *et al.* (2023).

The MHS and MWHS-2 instruments currently assimilated are aboard six different satellites (see Figure 1). However, as this work was done in parallel with testing the quality of FY-3E MWHS-2 data, these data are not included here. We do not investigate the thinning scale of data from the ATMS instrument, which is currently assimilated only in clear-sky conditions, or data from microwave imagers (SSMIS and GMI) which are superobbed.

5.1 Experimental setup

We perform experiments at two different IFS resolutions (Tco399 and Tco1279, approximately 28 and 9 km, respectively) to investigate whether the optimal thinning scale is sensitive to the model/analysis resolution. Table 4 lists the four inner loop resolutions used in the 4D-Var scheme for the two different outer loop resolutions. As can be seen, the final (highest resolution) inner loop used in the Tco399 experiment is equal to the first (coarsest resolution) inner loop used in the Tco1279 experiment. We use the same general experimental setup as detailed in section 3.1, but the dates are different. For the Tco399 resolution we perform experiments for summer (June to August 2021) and winter (December 2021 to February 2022). For the Tco1279 resolution we only perform experiments for the summer period. This is partly due to the large number of computing resources required and the long timeframe needed for the experiments to complete, but also because the Tco399 summer and winter experiments produced similar results. As such, we only show results for the summer period here.

We thin the MHS and MWHS-2 data to six different scales, as shown in Figure 14. To achieve these different thinning scales, two steps are required. In the first step, the data are thinned onto Gaussian grids with resolutions N128, N256 or N640, where the number specifies how many grid points there are between each pole and the equator. During this first thinning step, an observation has to lie within 25 km of the Gaussian grid point. If there are no observations within this distance, the grid point is unused. In the second optional step a 'diamond' thinning can be performed, in which every other Gaussian grid point is discarded, with this being staggered on each row to leave the data in a diamond pattern. This reduces the number of observations by a factor of two. The thinning scales we use range from the current operational value of $\sim$111 km (Figure 14a) to a nominal $\sim$16 km scale. Note that the cross-track spatial sampling for MHS and MWHS-2 ranges from 16 km at nadir to around 50 km at the edges of the swath,

	Tco399	Tco1279
Inner loop 1	TL95 (210 km)	TL255 (80 km)
Inner loop 2	TL159 (125 km)	TL319 (60 km)
Inner loop 3	TL255 (80 km)	TL399 (50 km)
Inner loop 4	TL255 (80 km)	TL511 (40 km)

Table 4: 4D-Var inner loop resolutions for the experiments performed at Tco399 and Tco1279 resolution, where Tco represents triangular–cubic-octahedral spectral truncation and TL represents triangular–linear truncation.

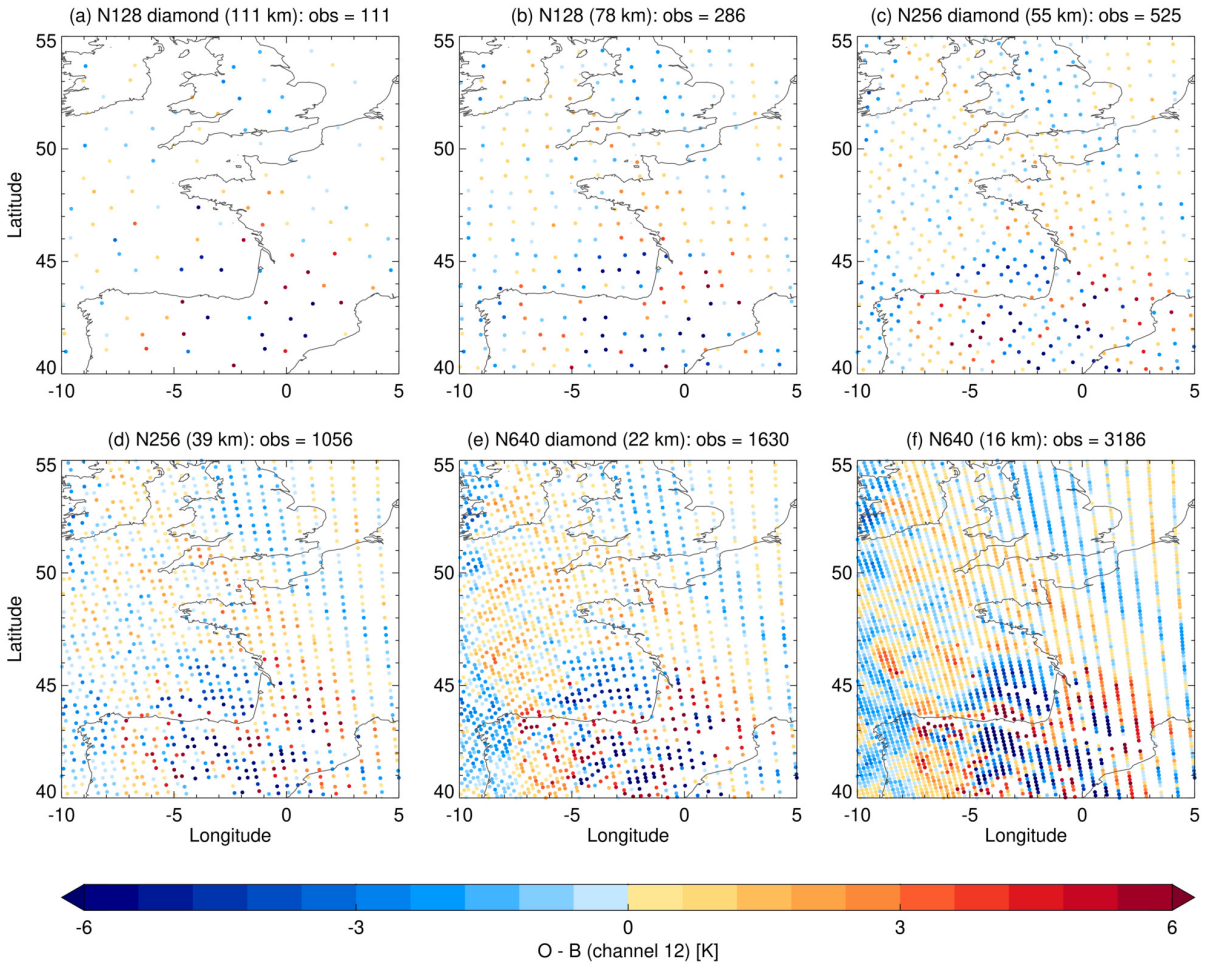

Figure 14: O–B from channel 12 of FY-3D MWHS-2 from a swath over western Europe on 1 June 2021. Panel (a) shows the current operational thinning scale of ∼111 km resolution, while subsequent panels reduce the thinning scale so that the number of observations roughly doubles.

so the nominal 16 km thinning implies using the observations at their native resolution. As seen in Figure 14, as the thinning scale reduces, an increased amount of spatial information is available.

5.2 Impact on short- and medium-range forecasts

We begin by looking at the impact on short-range 12 hour forecasts by comparing the O–B standard deviation, std(O–B), between the model and different observations, normalised by a control experiment that excludes MHS and MWHS-2 data. Figure 15 shows comparisons against a selection of different instruments. For each instrument, results from two pressure levels are shown. These levels were chosen based upon the quantity of observations available for robust statistics, and to show the general behaviour.

In terms of the impact on temperature (Figure 15a), the std(O–B) decreases for the lowest peaking ATMS channel assimilated (channel 6 with a weighting function peak at ∼600 hPa[4]). The improvement is greater in the higher-resolution (Tco1279) experiment, where a thinning scale of 39 km is optimal. In the lower-resolution (Tco399) experiment, the optimal thinning scale is larger, between 55–78 km. The reason for the worse performance at smaller thinning scales is likely due to spatial error correlations in the MHS and MWHS-2 observations that are unaccounted for. The better performance at Tco1279 may be related to the higher-resolution inner loops, allowing more spatial information to be extracted from the observations during the assimilation stage.

As the ATMS channels sample higher into the atmosphere the std(O–B) increases, with channels 9 and 10 (peaking at around 80–150 hPa) having the largest std(O–B). For these channels there is a slight improvement against the control for the 111 km thinning scale, but for all other thinning scales the performance is worse than the control which excludes the MHS and MWHS-2 instruments. However, as the channels continue to sample higher in the atmosphere, the std(O–B) begins to decrease again. For channel 14 which peaks at ∼5 hPa (not shown) there is an improvement compared to the control for thinning scales of 78 km at Tco399 and 55 km at Tco1279. This degradation and then improvement when moving upwards past the tropopause is also seen in comparisons against AMSU-A observations, and may be related to the generation of gravity waves in the model, but this will require further investigation.

The biggest improvement when altering the humidity sounder thinning scale can be seen when comparing against humidity-sensitive observations (Figure 15b,c). For ATMS we show channels 18 and 22, with weighting function peaks around 700 hPa and 400 hPa respectively. For SEVIRI we show the 6.2μm and 7.3μm water vapour bands, which have weighting function peaks at around 350 hPa and 500 hPa respectively[5]. Unlike for the ATMS temperature channels, all thinning scales produce an improvement compared to the control in the ATMS humidity channels. Comparisons against both ATMS and SEVIRI show that a thinning scale of ∼39 km is optimal, with the higher resolution model showing the biggest improvement. When comparing against the currently-used 111 km value, this leads to forecast improvements of ∼3% and ∼2% for ATMS and SEVIRI respectively. That the largest impact is seen in the ATMS humidity channels is perhaps unsurprising, given that ATMS uses the same frequencies as MHS and MWHS-2 (see Table 1).

For wind we compare against conventional wind observations (Figure 15d) and atmospheric motion vectors (AMVs; Figure 15e). Due to a much higher proportion of conventional wind observations being in the northern hemisphere (16 million vs 800,000 in the tropics and southern hemisphere), the results shown are most representative of this region. For both types of wind observation a similar picture

[4] https://www.star.nesdis.noaa.gov/star/documents/meetings/2015JPSSAnnual/dayOne/02_Session2_Weng_ATMS_SDR_Overview.pdf

[5] https://resources.eumetrain.org/data/Basic_Channels/print.htm

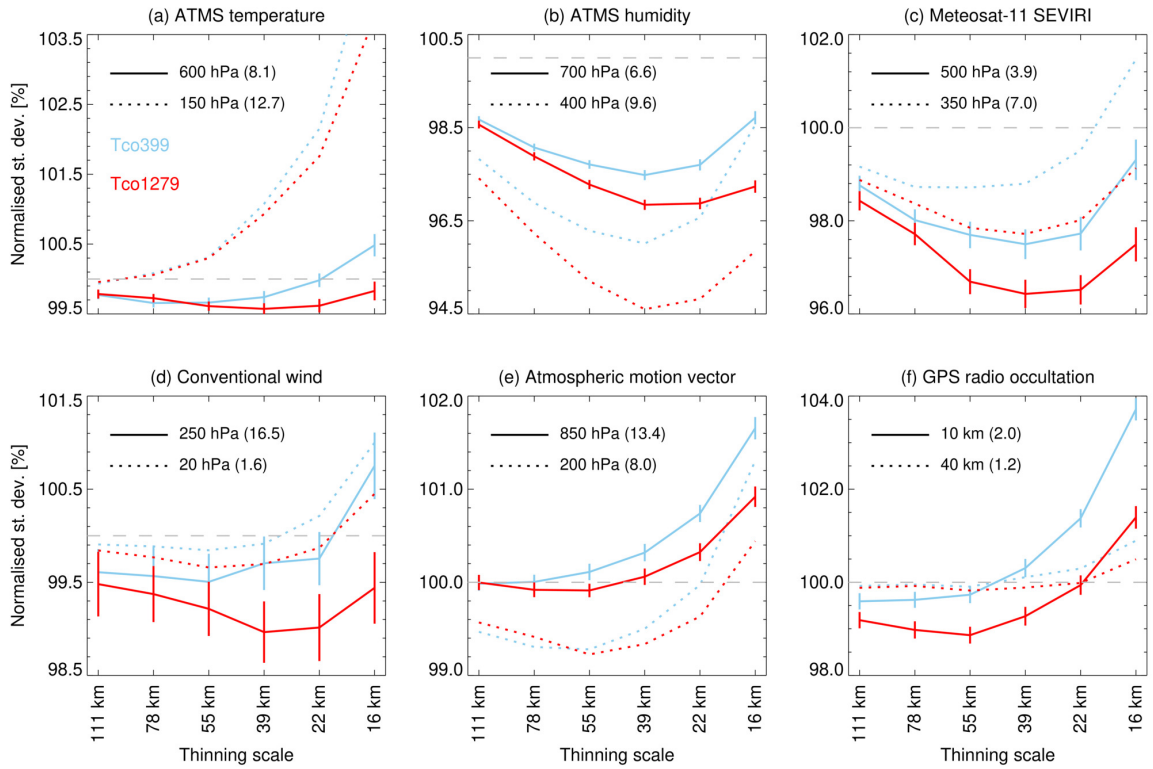

Figure 15: Impact of different microwave humidity sounder thinning scales on the O–B standard deviation (normalised by an experiment with no humidity sounders). Comparisons are made against six different instruments/channels, with values less than 100 representing short-range forecast improvements. Global data between June–August 2021 were used to calculate the statistics, with verification against the operational ECMWF analysis. Results are shown for experiments at Tco399 (blue) and Tco1279 (red) resolution, and at two different pressure/altitude levels (solid and dotted lines). Vertical lines show the 95% confidence range, and for clarity are only shown for one atmospheric level. The numbers in brackets represent the number of observations in millions. For ATMS (a,b) the quoted pressures represent the approximate level of the weighting function peak.

emerges, where (1) the higher-resolution Tco1279 experiment generally has a lower std(O–B), and (2) there is generally an improvement to the forecast as the thinning scale decreases, before it begins to degrade again as the smallest thinning scales are reached. Conventional wind observations show the largest improvement in the mid–upper troposphere (∼200–300 hPa) in the northern hemisphere and tropics, and in the lower troposphere (∼300–600 hPa) in the southern hemisphere. This difference may be related to the different seasons in each hemisphere, but may also be related to the lower density of observations in the southern hemisphere. AMVs show the largest improvement in the upper troposphere at around 150–250 hPa, with the lower troposphere showing much smaller improvements. For conventional wind the optimum thinning scale appears to be around 39 km and 55 km for Tco1279 and Tco399 respectively, while for AMVs the optimal thinning scale occurs at coarser values of 55 km and 78 km for Tco1279 and Tco399 respectively.

Finally, Figure 15f shows comparisons against GPS radio occultation measurements. In this case, large improvements occur over most of the troposphere in the higher-resolution Tco1279 experiment, with an optimal thinning scale of 55 km. In the lower-resolution Tco399 experiment little benefit is seen when altering the thinning scale from the currently-used value. As the altitude increases the impact of the thinning scale reduces, and by the time the mid-stratosphere is reached there is little difference between thinning scale or model resolution.

Another way to investigate the impact of altering the thinning scale, rather than looking at specific channels or atmospheric levels as in Figure 15, is to instead compute an average of the changes for each instrument over all channels or levels. For example, on ATMS the temperature-sounding channels 6–15, and humidity-sounding channels 18–22, are assimilated. For each thinning scale experiment, the normalised standard deviations for channels 6–15 and 18–22 can be averaged to obtain an overall impact on the temperature-sounding and humidity-sounding channels. The results of this averaging procedure can be seen in Figure 16. Across the bottom are the observation types, starting with surface and radio occultation observations, followed by blocks of wind-, humidity- and temperature-sensitive observations, and finishing with observations from microwave imagers. Blue shading shows where the average normalised background standard deviation is smaller than the control (signifying a short-range forecast improvement), while red shows a forecast degradation.

As can be seen, the humidity-sensitive observations have blue shading for nearly all thinning scales, with an optimal thinning scale of 39 km. The other observation types show forecast degradations for smaller thinning scales, with these degradations being worse in the Tco399 experiment. This again highlights the ability of the higher-resolution inner loops of the Tco1279 experiment to extract more useful information from denser observations. To balance the improvements seen for humidity-sensitive observations against the slight degradations for temperature- and wind-sensitive observations, thinning scales of around 78 km and 55 km appear most beneficial for resolutions of Tco399 and Tco1279 respectively.

In terms of the medium-range forecast impact, Figure 17 shows the normalised change in RMS error when comparing each thinning experiment against the control. This is similar to Figure 10, but rather than showing all 10 days of the forecast, results are shown just for day 3 at 200 hPa and 500 hPa, with similar behaviour seen over the 200–700 hPa range up to day 4. A larger impact is seen at 500 hPa, which may be related to the fact that the weighting functions for the humidity channels of MHS and MWHS-2 are closer to the surface (see Figure 3). Similar to what was seen for the short-range comparison against other instruments, Figure 17 suggests that the current global 111 km thinning scale can be improved by reducing it to around 78 km and 55 km for Tco399 and Tco1279 resolutions respectively.

While Figure 17 shows global results for two pressure levels, Figure 18 splits the 500 hPa results into three regions; the northern hemisphere, tropics and southern hemisphere. The 500 hPa level is representative of the general behaviour in the lower-middle troposphere, and is where the largest improvements are seen when altering the thinning scale. The exception is in the tropics where no one pressure level is representative of the behaviour of the geopotential height. As noted by Geer *et al.* (2014), this behaviour in the tropics does not appear when looking at changes in the standard deviation of forecast error instead of the RMS. It is caused by small changes in the mean analysed temperature in the tropics, which, in the absence of fast-growing random errors, makes changes in RMS errors tricky to interpret. For this reason, results for geopotential height in the tropics are not shown.

Looking at the higher resolution Tco1279 experiment first (Figure 18a–c) it can be seen that for a given thinning scale the improvements are largest in the extratropics compared to the tropics. Also, the error reduction is slightly larger in the northern hemisphere compared to the southern hemisphere, with this being more noticeable for the smallest thinning scales. The tropics tend to show little extra benefit from changing the thinning scale, and thus a value of $\sim$55 km, which improves the extratropics and doesn't degrade the tropics, seems a reasonable choice.

For the Tco399 experiment (Figure 18d–f) the extratropics again show a greater error reduction compared to the tropics. However, now it is generally the southern hemisphere that shows the largest error reduction, with the northern hemisphere showing a much more muted response. It is possible that there is a greater response in the northern hemisphere in the higher-resolution experiment due to the ability

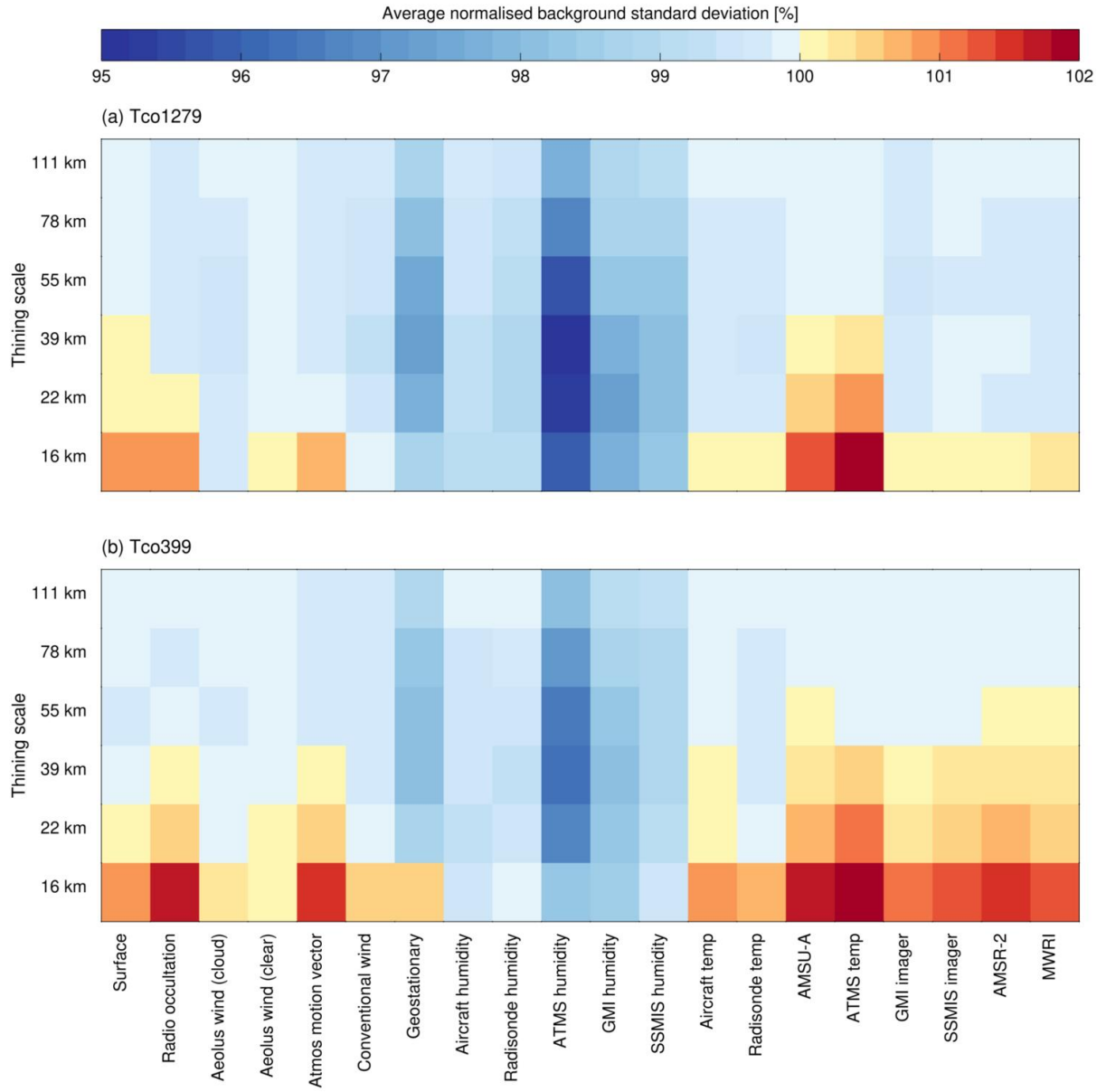

Figure 16: Average normalised background standard deviation for different thinning scales and instruments, for experiments at (a) Tco1279 resolution, and (b) Tco399 resolution. For each instrument the averages are calculated globally over all channels or all pressure/altitude levels, as appropriate. Statistics use global data between June–August 2021.

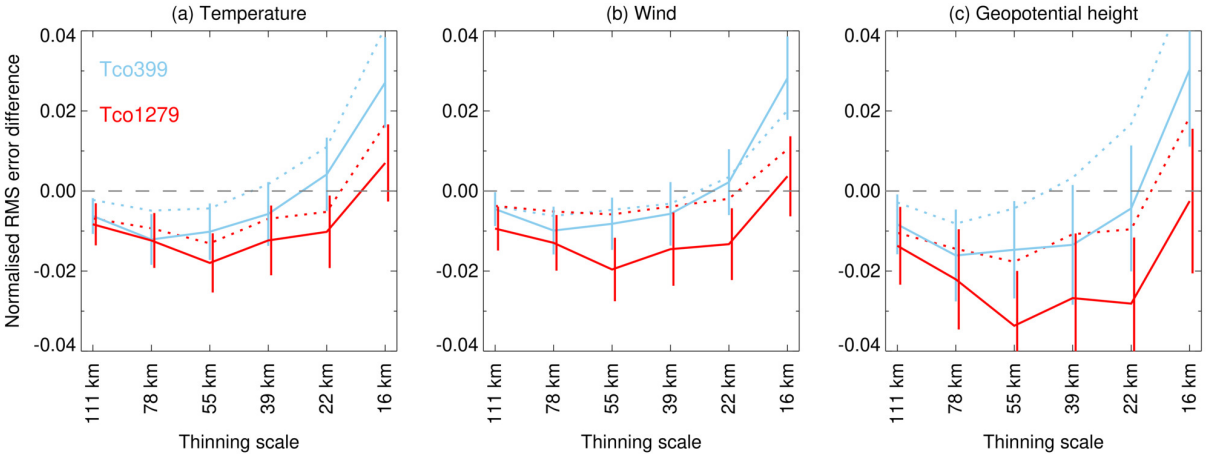

Figure 17: Normalised change in RMS error for different humidity sounder thinning scales at two different model resolutions, compared to the control. Results are shown for temperature, wind and geopotential height on forecast day 3 at 200 hPa (dotted line) and 500 hPa (solid line). Similar behaviour is seen over the 200–700 hPa range. Vertical lines show the 95% confidence range, and for clarity are only shown for 500 hPa. Statistics use global data between June–August 2021.

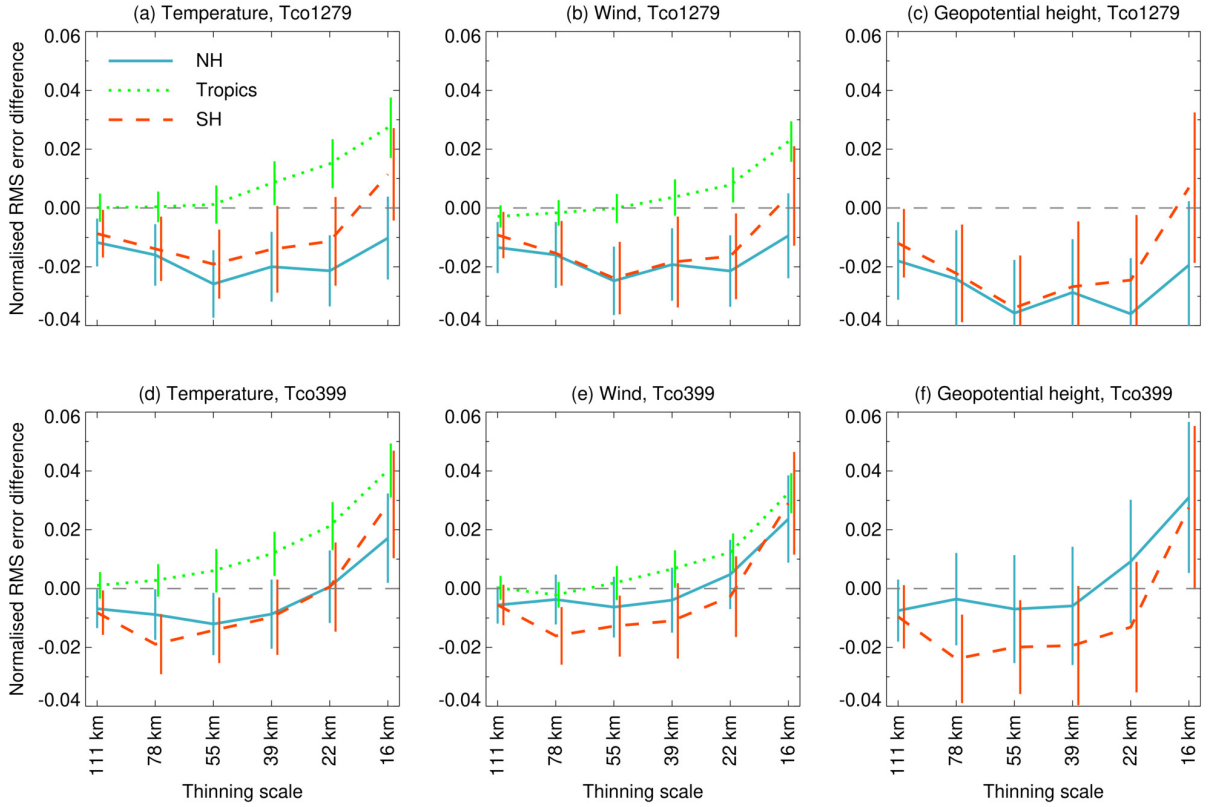

Figure 18: As Figure 17, but showing results at 500 hPa split into different regions for model resolutions of (a–c) Tco1279 and (d–f) Tco399. Results for geopotential height are not shown for the tropics, as there is a large variation depending on pressure level.

of the higher-resolution inner loops of the 4D-Var scheme to extract more information from the humidity sounder observations. In the lower-resolution experiment the humidity sounder observations may be having a larger impact in the southern hemisphere where there is a lack of non-satellite observations, but having a reduced impact in the northern hemisphere where there is a wealth of other different observation types to constrain the assimilation. Due to the more muted error reduction in the northern hemisphere there is a less clear choice for the optimal thinning scale here. However, a value of 78 km is optimal for the southern hemisphere, and this also gives an error reduction in the northern hemisphere and doesn't degrade the forecast in the tropics, so this seems a suitable value.

The results here show that there are similarities between the behaviour at the two different model resolutions tested, with benefits seen when moving towards a smaller thinning scale than currently used, before degradations begin to appear for the smallest thinning scales. Thus, for research experiments performed at Tco399 resolution, much of the general behaviour that will appear in the operational forecast is captured. This is good news, as the lower-resolution experiments are much quicker to perform, and much less costly in terms of computing resources. However, not all the features seen at higher resolution are captured. For example, the improvement in the northern hemisphere seen at Tco1279 is missing at Tco399. Thus, for more detailed investigations into the precise thinning scales to use, it is necessary to perform research experiments at the operational resolution.

The likely cause for the degradation seen at the smaller thinning scales is the lack of spatial error correlations. Were these to be taken into consideration, it may be possible to reduce the thinning scale further, as it is clear that the observations contain much more information that we are able to extract from 4D-Var (see Figure 14). However, an assessment would need to be made with regards to the benefits of using smaller thinning scales and correlated errors versus the increased computing cost required.

6 Conclusions

In this study we have (1) examined the quality of data from the microwave humidity sounding MWHS-2 instrument on the FY-3E satellite, (2) investigated whether there is any forecast benefit from assimilating this data in ECMWFs Integrated Forecasting System, and (3) investigated the optimal thinning scale for microwave humidity sounder data.

O–B statistics for 'clear-sky' data were used to assess the quality of the FY-3E MWHS-2 data. Standard deviations of background departures indicate a clear improvement in the instrument noise performance of the 118 GHz-channels of FY-3E compared to the predecessors, whereas the noise performance of other channels is overall comparable. Biases for the MWHS-2 humidity channels on FY-3E (before bias correction has been applied) are smaller compared to FY-3C and FY-3D, whereas a more consistent (negative) bias is present in the temperature-sounding channels. The outer two scan positions on each edge of the swath display large biases in FY-3E MWHS-2, and so these are removed. After this removal the biases (after bias correction) are overall close to zero for most channels. The only outlier is channel 7, which displays an 'm-shaped' bias pattern in the scan position which is more difficult to correct with our current approach of using a third order polynomial.

As the FY-3E MWHS-2 data quality appeared good compared to similar instruments, assimilation experiments were performed between 11 October 2022 and 28 February 2023. The experiment results showed improvements in both the short-range 12 hour forecasts (when comparing against independent observations) and also in the medium range, out to day 3, when verified against operational analyses. The largest benefits are seen in the southern hemisphere, where temperature, wind and geopotential height are improved by $\sim$0.6–0.8%. Because of the results of the data quality assessment and assimilation ex-

periments, it was decided to include FY-3E MWHS-2 in the operational forecast, and the sensor became active on 22 February 2023. Experiments performed by Duncan and Bormann (2020) found that continued benefit is seen when adding new microwave sensors, and that saturation has not yet been reached. Thus, it is likely that assimilating additional microwave sounders in the future will continue to bring forecast benefits.

Additional assimilation experiments demonstrate the benefit of adding data in an uncovered orbit compared to adding data in an orbit that is already well-covered by other satellites. Assimilating MWHS-2 data from FY-3E in the otherwise uncovered early-morning orbit has a larger impact than assimilating MWHS-2 data from FY-3D, which is in an afternoon orbit similar to S-NPP and NOAA-20. This result was from experiments restricted to only humidity channels that show similar performance on both satellites, and thus the impact of also including the temperature-sounding channels would likely be larger. This is in line with previous studies that motivated the use of the early-morning orbit for FY-3E (di Tomaso and Bormann, 2011; WMO-CGMS Tiger Team, 2013; Eyre and Weston, 2014). It also highlights in general the benefit to NWP of complementary equator crossing times, an aspect that has been taken on board in the design of the EPS-Sterna constellation[6]. There are additional instruments on board FY-3E that we did not assimilate in the experiments performed here, such as the Micro-Wave Temperature Sounder - 3 and the Hyperspectral Infrared Atmospheric Sounder - 2. Thus, it is likely that there will be even more impact from the complementary FY-3E orbit once work begins to assimilate these additional data.

Finally, investigations were performed to assess the optimal spatial thinning scale to use for microwave humidity-sounding observations. This is to enable us to obtain the most benefit from the observations we currently assimilate, as well as observations we plan to assimilate in the future, such as those from the Microwave Sounder on EUMETSATs Metop second generation satellites and the microwave radiometer on the EPS-Sterna constellation. Experiments were performed with thinning scales ranging from the current operational value of ∼111 km down to ∼16 km, which corresponds to all the observations being used. Benefits out to forecast day 4 are observed when the thinning scale is reduced to ∼78 km for Tco399 experiments, and ∼55 km for Tco1279 experiments. The optimal thinning scales found here are smaller than those of ∼115-154 km found by Dando *et al.* (2007). However, there are a number of differences in the model and assimilation schemes. Dando *et al.* (2007) used the Met Office model with 60 km resolution, a 3D-Var assimilation scheme with a 6 hour window, and with experiments ranging from 5 days to 3 weeks. Additionally, only clear-sky data were used. The lower resolution model, assimilation scheme that doesn't account for time evolution within the assimilation window, and use of cloud- and precipitation-free observations over short periods of time is likely why a larger thinning scale was favoured. Indeed, Dando *et al.* (2007) noted that regions such as frontal systems with larger gradients benefit from smaller thinning scales, and the higher-resolution model used for our experiments will be able to better capture such gradients. For the smallest thinning scales in our experiments there are still benefits observed in the model humidity field, but degradations appear in the temperature and wind fields, likely due to neglected spatial observation error correlations. The results highlight the need for revisiting thinning choices as the resolution of assimilation systems increases. Note that the thinning scales for MHS and MWHS-2 are going to be updated in cycle 49r1 of the ECMWF system, to be implemented in 2024, adopting a thinning scale of 70 km, combined with superobbing to 50 km resolution (Duncan *et al.*, 2023). Due to the reduction in noise seen when superobbing, especially for the 183 GHz channels of MWHS-2, it may be useful to repeat some of the thinning experiments performed here with the addition of superobbing.

[6] https://www.eumetsat.int/eumetsat-invests-development-new-weather-and-climate-satellite-systems

Acknowledgements

Liam Steele is funded by the EUMETSAT Fellowship Programme. Thanks to Alan Geer and Peter Lean for help with the experiments and analysis.

References

Auligné, T., McNally, A. P. and Dee, D. P. (2007). Adaptive bias correction for satellite data in a numerical weather prediction system. *Quarterly Journal of the Royal Meteorological Society*, **133**(624), 631–642, doi:10.1002/qj.56.

Baordo, F. and Geer, A. J. (2016). Assimilation of SSMIS humidity-sounding channels in all-sky conditions over land using a dynamic emissivity retrieval. *Quarterly Journal of the Royal Meteorological Society*, **142**(700), 2854–2866, doi:10.1002/qj.2873.

Bauer, P., Moreau, E., Chevallier, F. and O'Keeffe, U. (2006). Multiple-scattering microwave radiative transfer for data assimilation applications. *Quarterly Journal of the Royal Meteorological Society*, **132**(617), 1259–1281, doi:10.1256/qj.05.153.

Bormann, N., Duncan, D., English, S., Healy, S., Lonitz, K., Chen, K., Lawrence, H. and Lu, Q. (2021). Growing Operational Use of FY-3 Data in the ECMWF System. *Advances in Atmospheric Sciences*, **38**(8), 1285–1298, doi:10.1007/s00376-020-0207-3.

Carminati, F. and Migliorini, S. (2021). All-sky Data Assimilation of MWTS-2 and MWHS-2 in the Met Office Global NWP System. *Advances in Atmospheric Sciences*, **38**(10), 1682–1694, doi:10.1007/s00376-021-1071-5.

Chen, K., Chen, Z., Xian, Z. and Li, G. (2023). Impacts of the All-Sky Assimilation of FY-3C and FY-3D MWHS-2 Radiances on Analyses and Forecasts of Typhoon Hagupit. *Remote Sensing*, **15**(9), 2279, doi:10.3390/rs15092279.

Dando, M. L., Thorpe, A. J. and Eyre, J. R. (2007). The optimal density of atmospheric sounder observations in the Met Office NWP system. *Quarterly Journal of the Royal Meteorological Society*, **133**(629), 1933–1943, doi:10.1002/qj.175.

di Michele, S. and Bauer, P. (2006). Passive microwave radiometer channel selection based on cloud and precipitation information content. *Quarterly Journal of the Royal Meteorological Society*, **132**(617), 1299–1323, doi:10.1256/qj.05.164.

di Tomaso, E. and Bormann, N. (2011). *Assimilation of ATOVS radiances at ECMWF: first year EUMETSAT fellowship report*. Shinfield Park, Reading, URL https://www.ecmwf.int/node/9049.

Duncan, D. and Bormann, N. (2020). On the addition of microwave sounders and NWP skill, including assessment of FY-3D sounders. *Technical Report 55*, EUMETSAT/ECMWF Fellowship Programme Research Report, doi:10.21957/iimhohmqt, URL https://www.ecmwf.int/node/19760.

Duncan, D., Bormann, N., Geer, A. and Weston, P. (2023). Superobbing and finer thinning for all-sky humidity sounder assimilation. doi:10.21957/5c3b9c8d9f, URL .

Duncan, D. I., Bormann, N. and Hólm, E. V. (2021). On the addition of microwave sounders and numerical weather prediction skill. *Quarterly Journal of the Royal Meteorological Society*, **147**(740), 3703–3718, doi:10.1002/qj.4149.

Eyre, J. R. and Weston, P. P. (2014). The impact of the temporal spacing of observations on analysis errors in an idealised data assimilation system. *Quarterly Journal of the Royal Meteorological Society*, **140**(682), 1441–1452, doi:10.1002/qj.2227.

Geer, A. (2013). All-sky assimilation: better snow-scattering radiative transfer and addition of ssmis humidity sounding channels. doi:10.21957/uxq5zlprk, URL https://www.ecmwf.int/node/9502.

Geer, A., Baordo, F., Bormann, N. and English, S. (2014). All-sky assimilation of microwave humidity sounders. doi:10.21957/obosmx154, URL https://www.ecmwf.int/node/9507.

Geer, A., Lonitz, K., Duncan, D. and Bormann, N. (2022). Improved surface treatment for all-sky microwave observations. doi:10.21957/zi7q6hau, URL https://www.ecmwf.int/node/20337.

Geer, A. J. (2016). Significance of changes in medium-range forecast scores. *Tellus Series A*, **68**, 30229, doi:10.3402/tellusa.v68.30229.

Geer, A. J. (2021). Physical characteristics of frozen hydrometeors inferred with parameter estimation. *Atmospheric Measurement Techniques*, **14**(8), 5369–5395, doi:10.5194/amt-14-5369-2021.

Geer, A. J., Baordo, F., Bormann, N., Chambon, P., English, S. J., Kazumori, M., Lawrence, H., Lean, P., Lonitza, K. and Lupu, C. (2017). The growing impact of satellite observations sensitive to humidity, cloud and precipitation. *Quarterly Journal of the Royal Meteorological Society*, **143**(709), 3189–3206, doi:10.1002/qj.3172.

Geer, A. J. and Bauer, P. (2011). Observation errors in all-sky data assimilation. *Quarterly Journal of the Royal Meteorological Society*, **137**(661), 2024–2037, doi:10.1002/qj.830.

Geer, A. J., Bauer, P., Lonitz, K., Barlakas, V., Eriksson, P., Mendrok, J., Doherty, A., Hocking, J. and Chambon, P. (2021). Bulk hydrometeor optical properties for microwave and sub-millimetre radiative transfer in RTTOV-SCATT v13.0. *Geoscientific Model Development*, **14**(12), 7497–7526, doi:10.5194/gmd-14-7497-2021.

Hoffman, R. N. (2018). The Effect of Thinning and Superobservations in a Simple One-Dimensional Data Analysis with Mischaracterized Error. *Monthly Weather Review*, **146**(4), 1181–1195, doi:10.1175/MWR-D-17-0363.1.

Jiang, L., Shi, C., Zhang, T., Guo, Y. and Yao, S. (2020). Evaluation of Assimilating FY-3C MWHS-2 Radiances Using the GSI Global Analysis System. *Remote Sensing*, **12**(16), 2511, doi:10.3390/rs12162511.

Kan, W., Dong, P., Weng, F., Hu, H. and Dong, C. (2022). Impact of Fengyun-3E Microwave Temperature and Humidity Sounder Data on CMA Global Medium Range Weather Forecasts. *Remote Sensing*, **14**(19), 5014, doi:10.3390/rs14195014.

Kim, M.-J., Jin, J., El Akkraoui, A., McCarty, W., Todling, R., Gu, W. and Gelaro, R. (2020). The Framework for Assimilating All-Sky GPM Microwave Imager Brightness Temperature Data in the NASA GEOS Data Assimilation System. *Monthly Weather Review*, **148**(6), 2433–2455, doi:10.1175/MWR-D-19-0100.1.

Lawrence, H., Bormann, N., Geer, A. and English, S. (2015). *An Evaluation of FY-3C MWHS-2 at ECMWF*. Shinfield Park, Reading, URL https://www.ecmwf.int/node/10668.

Lawrence, H., Bormann, N., Geer, A. J., Lu, Q. and English, S. J. (2018). Evaluation and Assimilation of the Microwave Sounder MWHS-2 Onboard FY-3C in the ECMWF Numerical Weather Prediction System. *IEEE Transactions on Geoscience and Remote Sensing*, **56**(6), 3333–3349, doi:10.1109/TGRS.2018.2798292.

Lean, P., Geer, A. and Lonitz, K. (2017). Assimilation of global precipitation mission (gpm) microwave imager (gmi) in all-sky conditions. doi:10.21957/8orc7sn33, URL https://www.ecmwf.int/node/17174.

Liu, R., Lu, Q., Chen, M., Mao, L. and Fan, S. (2021). Impact of assimilating FY-3C MWHS2 data in the RMAPS-ST forecast system on its rainfall forecasts. *Atmospheric and Oceanic Science Letters*, **14**, 100059, doi:10.1016/j.aosl.2021.100059.

Liu, Z. Q. and Rabier, F. (2002). The interaction between model resolution, observation resolution and observation density in data assimilation: A one-dimensional study. *Quarterly Journal of the Royal Meteorological Society*, **128**(582), 1367–1386, doi:10.1256/003590002320373337.

Liu, Z. Q. and Rabier, F. (2003). The potential of high-density observations for numerical weather prediction: A study with simulated observations. *Quarterly Journal of the Royal Meteorological Society*, **129**(594), 3013–3035, doi:10.1256/qj.02.170.

Lopez, P. and Moreau, E. (2005). A convection scheme for data assimilation: Description and initial tests. *Quarterly Journal of the Royal Meteorological Society*, **131**(606), 409–436, doi:10.1256/qj.04.69.

Ma, S., Zhang, W., Cao, X., Zhao, Y. and Liu, B. (2022). Assimilation of All-Sky Radiance from the FY-3 MWHS-2 with the Yinhe 4D-Var System. *Journal of Meteorological Research*, **36**(5), 750–766, doi:10.1007/s13351-022-1208-1.

Maddy, E. S., Bunin, S., Mikles, V. J., Shahroudi, N., Shiotani, B. and Boukabara, S.-A. (2022). Temperature and Moisture Sounding Performance of Current and Prospective Microwave Instruments under All-Sky Conditions. *Remote Sensing*, **14**(7), 1624, doi:10.3390/rs14071624.

Mallick, S. (2022). Impact of adaptively thinned goes-16 cloud water path in an ensemble data assimilation system. *Meteorology*, **1**(4), 513–530, URL https://www.mdpi.com/2674-0494/1/4/32.

Mao, J., Qin, Z., Li, J., Han, Y. and Huang, J. (2022). Performance Evaluation and Noise Mitigation of the FY-3E Microwave Humidity Sounder. *Remote Sensing*, **14**(19), 4835, doi:10.3390/rs14194835.

Ochotta, T., Gebhardt, C., Saupe, D. and Wergen, W. (2005). Adaptive thinning of atmospheric observations in data assimilation with vector quantization and filtering methods. *Quarterly Journal of the Royal Meteorological Society*, **131**(613), 3427–3437, doi:10.1256/qj.05.94.

Peubey, C. and McNally, A. P. (2009). Characterization of the impact of geostationary clear-sky radiances on wind analyses in a 4D-Var context. *Quarterly Journal of the Royal Meteorological Society*, **135**(644), 1863–1876, doi:10.1002/qj.500.

Stewart, L. M., Dance, S. L. and Nichols, N. K. (2008). Correlated observation errors in data assimilation. *International Journal for Numerical Methods in Fluids*, **56**(8), 1521–1527, doi:10.1002/fld.1636.

Tompkins, A. M. and Janisková, M. (2004). A cloud scheme for data assimilation: Description and initial tests. *Quarterly Journal of the Royal Meteorological Society*, **130**(602), 2495–2517, doi:10.1256/qj.03.162.

WMO-CGMS Tiger Team (2013). Assessment of the benefits of a satellite mission in an early morning orbit. URL https://library.wmo.int/idurl/4/49699.

Xian, Z., Chen, K. and Zhu, J. (2019). All-Sky Assimilation of the MWHS-2 Observations and Evaluation the Impacts on the Analyses and Forecasts of Binary Typhoons. *Journal of Geophysical Research (Atmospheres)*, **124**(12), 6359–6378, doi:10.1029/2018JD029658.

Xiao, H., Han, W., Zhang, P. and Bai, Y. (2023). Assimilation of data from the MWHS-II onboard the first early morning satellite FY-3E into the CMA global 4D-Var system. *Meteorological Applications*, **30**(3), 2133, doi:10.1002/met.2133.

Zhang, P., Hu, X., Lu, Q., Zhu, A., Lin, M., Sun, L., Chen, L. and Xu, N. (2022). FY-3E: The First Operational Meteorological Satellite Mission in an Early Morning Orbit. *Advances in Atmospheric Sciences*, **39**(1), 1–8, doi:10.1007/s00376-021-1304-7.